

FINE-STRUCTURE FE II* EMISSION AND RESONANT MG II EMISSION IN $z \sim 1$ STAR-FORMING GALAXIES¹

KATHERINE A. KORNEI AND ALICE E. SHAPLEY²

Department of Physics and Astronomy, University of California, Los Angeles, CA 90025, USA

CRYSTAL L. MARTIN

Physics Department, University of California, Santa Barbara, CA 93106, USA

ALISON L. COIL³

Center for Astrophysics and Space Sciences, Department of Physics, University of California, San Diego, CA 92093, USA

JENNIFER M. LOTZ

Space Telescope Science Institute, Baltimore, MD 21218, USA

BENJAMIN J. WEINER

Steward Observatory, University of Arizona, Tucson, AZ 85721, USA

Draft version February 8, 2018

ABSTRACT

We present a study of the prevalence, strength, and kinematics of ultraviolet Fe II and Mg II emission lines in 212 star-forming galaxies at $z \sim 1$ selected from the DEEP2 survey. We find Fe II* emission in composite spectra assembled on the basis of different galaxy properties, indicating that Fe II* emission is common at $z \sim 1$. In these composites, Fe II* emission is observed at roughly the systemic velocity. At $z \sim 1$, we find that the strength of Fe II* emission is most strongly modulated by dust attenuation, and is additionally correlated with redshift, star-formation rate, and [O II] equivalent width, such that systems at higher redshifts with lower dust levels, lower star-formation rates, and larger [O II] equivalent widths show stronger Fe II* emission. We detect Mg II emission in at least 15% of the individual spectra and we find that objects showing stronger Mg II emission have higher specific star-formation rates, smaller [O II] linewidths, larger [O II] equivalent widths, lower dust attenuations, and lower stellar masses than the sample as a whole. Mg II emission strength exhibits the strongest correlation with specific star-formation rate, although we find evidence that dust attenuation and stellar mass also play roles in the regulation of Mg II emission. Future integral field unit observations of the spatial extent of Fe II* and Mg II emission in galaxies with high specific star-formation rates, low dust attenuations, and low stellar masses will be important for probing the morphology of circumgalactic gas.

1. INTRODUCTION

The transport of gas into and out of galaxies has been recorded at a range of redshifts (e.g., Heckman et al. 1990; Steidel et al. 1996; Franx et al. 1997; Martin 1999; Pettini et al. 2000, 2001; Shapley et al. 2003; Martin 2005; Veilleux et al. 2005; Rupke et al. 2005; Tremonti et al. 2007; Weiner et al. 2009; Steidel et al. 2010; Coil et al. 2011). This cycling of baryons is an integral component of galaxy evolution as galactic winds are thought to drive the mass-metallicity relation (e.g., Tremonti et al. 2004; Erb et al. 2006), enrich the intergalactic medium in metals (e.g., Bordoloi et al. 2011; Ménard et al. 2011), and regulate both star formation and black hole growth (e.g., Tremonti et al. 2007;

Gabor et al. 2011).

In the local universe, galactic winds are revealed through H α and X-ray imaging of high surface brightness gas seen in emission around the disks of starburst galaxies (e.g., Lehnert & Heckman 1996). At higher redshifts, however, studies of galactic winds often rely on spectral data tracing foreground gas absorbed against the light of background galaxies or quasars (e.g., Sato et al. 2009; Weiner et al. 2009; Steidel et al. 2010; Rubin et al. 2010b; Coil et al. 2011). While absorption lines unambiguously probe gas between Earth and a more distant light source, emission lines can arise from either foreground or background gas due to scattering. Observations of emission lines associated with galactic winds can be used to map the spatial extent of circumgalactic gas (e.g., Rubin et al. 2011) and measurements of emission lines accordingly comprise rich data sets complementing absorption-line studies.

The H I Ly α line at 1216 Å is an example of a well-studied resonant feature associated with galactic winds.

¹ Based, in part, on data obtained at the W.M. Keck Observatory, which is operated as a scientific partnership among the California Institute of Technology, the University of California, and NASA, and was made possible by the generous financial support of the W.M. Keck Foundation.

² Packard Fellow.

³ Alfred P. Sloan Fellow.

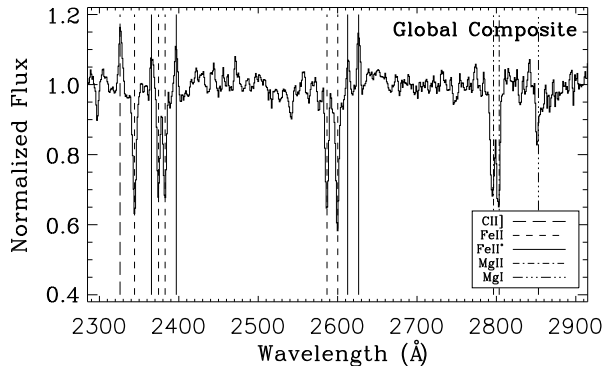


FIG. 1.— Composite spectrum of all the data in our sample. Prominent interstellar absorption lines (Fe II, Mg II, and Mg I) and emission lines (C II], fine-structure Fe II*) are labeled, where the C II] line is a blend of several features and we mark a wavelength of 2326 Å in the figure. The absorption line at 2297 Å is a stellar C III line. The S/N of this composite spectrum is ~ 39 pixel $^{-1}$.

This line has been observed in emission at $z \sim 3$ in star-forming galaxies (Shapley et al. 2003). At lower redshifts, Mg II resonant emission at ~ 2800 Å or Na I D resonant emission at ~ 5900 Å are typically used as emission-line probes of galactic winds. One of the first spectroscopic observations of resonant emission associated with outflowing gas was a Na I P-Cygni profile in the local starburst galaxy NGC 1808 (Phillips 1993), although recombination features have also been used as tracers of galactic winds (e.g., Heckman et al. 1990; Martin 1998; Genzel et al. 2011). Fine-structure emission – in which a photon is emitted following an electronic transition to an excited ground state – is necessarily related to resonant emission lines as the upper electronic states of both kinds of features are populated by resonant absorption. Examples of fine-structure emission lines include Si II* and Fe II* features, where we adopt the convention of denoting fine-structure lines with an asterisk. In this paper, we present observations of Fe II* emission at $z \sim 1$ to study its prevalence and kinematics. Many authors have noted resonant and fine-structure emission lines in diverse samples of star-forming galaxies at $0.3 < z < 4$ hosting galactic winds (Shapley et al. 2003; Martin & Bouché 2009; Weiner et al. 2009; Rubin et al. 2010b, 2011; Coil et al. 2011; Kornei et al. 2012; Martin et al. 2012; Jones et al. 2012; Talia et al. 2012; Erb et al. 2012).

While kinematic measurements of emission lines should in principle be a useful diagnostic of the origin of the line-emitting gas, work by Prochaska et al. (2011) has shown that it is difficult to determine if emission lines arise from galactic winds or star-forming regions. These authors propose that gas flows and stationary H II regions can imprint similar kinematic signatures on line emission. As emission from an optically thin source will be visible over both its approaching and receding (i.e., blueshifted and redshifted) sides, the emission profile can remain centered at roughly 0 km s $^{-1}$ while still tracing a gas flow. Likewise, an emission line arising from a stationary H II region will exhibit a line profile largely at the systemic velocity. Rubin et al. (2011) investigated fine-structure Fe II* emission in a starburst galaxy at $z \sim 0.7$ and concluded that since the emission was red-

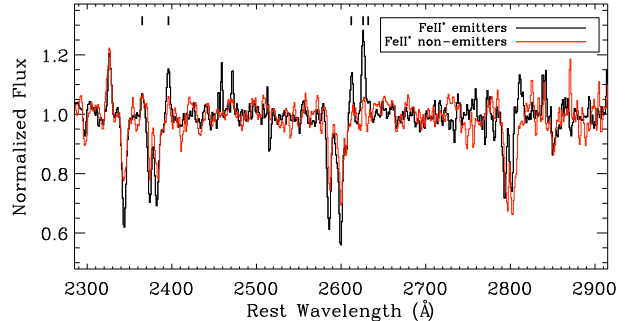


FIG. 2.— A comparison of composite spectra assembled from Fe II* emitters (black) and non-emitters (red). Short vertical lines delineate the locations of Fe II* emission features at 2365, 2396, 2612, 2626, and 2632 Å; the emission feature at 2326 Å is a blend of several C II] transitions. On average, Fe II* emitters show deeper Fe II absorption, weaker Mg II absorption, and more blueshifted Mg II absorption than Fe II* non-emitters.

ward or within 30 km s $^{-1}$ of the systemic velocity, the velocity profile of fine-structure Fe II* emission is significantly different from both absorption lines tracing galactic winds and nebular lines associated with H II regions. Coil et al. (2011) reported that the Fe II* emission lines in a sample of 11 post-starburst and active galactic nucleus (AGN) host galaxies at $0.2 < z < 0.8$ are within 2σ of the systemic velocity for all but two galaxies. At higher redshift, Erb et al. (2012) studied 96 star-forming galaxies at $1 \lesssim z \lesssim 2$ and found that the measured velocities of fine-structure Fe II* emission scattered around 0 km s $^{-1}$ and that the similarity of the Fe II* and Fe II line profiles indicate that the lines arise from the same gas. At $z \sim 3$, Shapley et al. (2003) measured an average velocity of 100 ± 35 km s $^{-1}$ for fine-structure Si II* emission, although these authors cautioned that the presence of nearby absorption features may bias the emission centroids to more redshifted values. While these collective measurements have shown that fine-structure emission is generally observed at or near the systemic velocity, additional data obtained with higher resolution spectrographs are needed in order to more precisely investigate the kinematics of fine-structure emission.

The prevalence of emission lines has been found to vary widely among different samples, with objects at higher redshifts more commonly exhibiting emission lines. Studies at $0.5 < z < 4$ have detected fine-structure Si II*, fine-structure Fe II*, and resonant Mg II emission lines (e.g., Shapley et al. 2003; Weiner et al. 2009; Rubin et al. 2010b; Kurk et al. 2013; Jones et al. 2012). In a study of 1406 star-forming galaxies at $z \sim 1.4$, Weiner et al. (2009) found that $\sim 4\%$ of objects showed excess Mg II emission; these authors attributed the presence of Mg II emission to either low-level AGNs⁴ or scattering off the backside of the galactic wind. Rubin et al. (2011) detected both Fe II* and Mg II emission in a starburst galaxy at $z \sim 0.7$ and measured that the Mg II emission was spatially extended to distances of ~ 7 kpc. Local star-forming galaxies, on the other hand, do not show fine-structure emission lines (Leitherer et al. 2011).

⁴ Weiner et al. (2009) still observed Mg II emission, however, in a sample where the AGN candidates had been removed.

Giavalisco et al. (2011) and Erb et al. (2012), among others, suggest that slit losses are responsible for the lack of emission in nearby samples, given that spectroscopic observations in the local universe typically probe only the inner regions of galaxies where the emission may not originate.

While previous studies have collectively shown that emission lines are present in galaxies at $z \gtrsim 0.5$ exhibiting galactic winds, a systematic analysis of the prevalence and properties of emission lines as a function of host galaxy stellar populations, star-formation rate (SFR), SFR surface density, and outflow characteristics has thus far been absent from the literature. We present here an investigation of the frequency, strength, and kinematics of rest-frame ultraviolet fine-structure Fe II* and resonant Mg II emission lines in a sample of 212 galaxies at $0.2 < z < 1.3$ (all but four of which are at $z > 0.4$) for which stellar populations and outflow properties have been estimated. In Section 2, we present the observations and in Section 3 we discuss how outflow velocities were measured. Section 4 summarizes the Fe II* emission features seen in the data while Section 5 is devoted to Mg II emission observations. A discussion appears in Section 6 and conclusions are presented in Section 7. Throughout the paper, we assume a standard Λ CDM cosmology with $H_0 = 70 \text{ km s}^{-1} \text{ Mpc}^{-1}$, $\Omega_M = 0.3$, and $\Omega_\Lambda = 0.7$. All wavelengths are measured in vacuum. At $z = 0.7$ (1.3), an angular size of $1''$ corresponds to 7.1 (8.4) kpc.

2. OBSERVATIONS

We discuss the details of our observations in Martin et al. (2012). The 212 objects in our sample are drawn from the DEEP2 survey (Newman et al. 2012) utilizing the DEep Imaging Multi-Object Spectrograph (DEIMOS) on Keck II. While the DEIMOS spectra are generally dominated by nebular emission features, the majority of low- and high-ionization interstellar absorption features tracing outflows are in the rest-frame ultraviolet and are observed at shorter wavelengths than the blue edge of the typical DEIMOS spectra ($\sim 6500 \text{ \AA}$ in the observed frame). In order to probe these outflow features (e.g., Fe II $\lambda 2344$, Fe II $\lambda \lambda 2374, 2382$, Fe II $\lambda \lambda 2587, 2600$, Mg II $\lambda \lambda 2796, 2803$), we obtained spectroscopic data using the LRIS spectrograph on Keck I.

These LRIS data are described in detail in Martin et al. (2012) and we provide here only a summary. The published Martin et al. (2012) sample is inclusive of 208 galaxies; we include four additional low-redshift galaxies in this work to bring the sample total to 212 objects. The LRIS data were collected from 2007–2010 using $1.''2$ slits on multi-object slitmasks targeting 20–28 objects each. We used two set-up configurations, both with the atmospheric dispersion corrector: the d680 dichroic with the 400 line mm^{-1} grism and the 800 line mm^{-1} grating (145 objects) and the d560 dichroic with the 600 line mm^{-1} grism and the 600 line mm^{-1} grating (67 objects). Integration times ranged from 3–9 hours per slitmask, where objects observed with the d560 dichroic had typically shorter exposures (3–5 hours) than objects observed with the d680 dichroic (5–9 hours). The slitmasks used with the d560 dichroic were reserved for brighter objects observed in poorer conditions. The resolutions of the 800 , 600 and 400 line mm^{-1} gratings/grisms are $R = 2000$, 1100 , and 700 , respec-

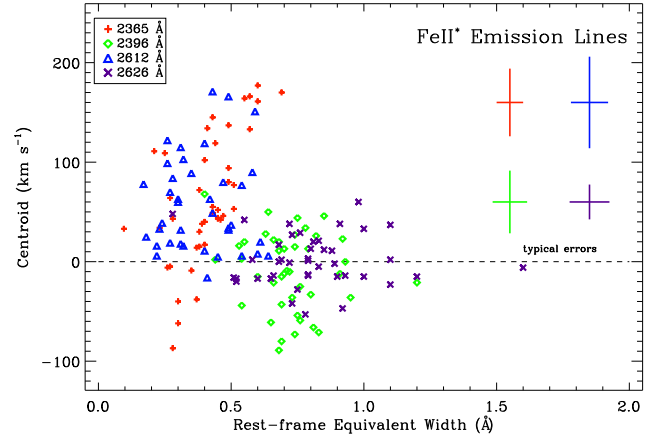


FIG. 3.— Fe II* kinematics versus equivalent width for a set of high S/N composite spectra assembled according to different galaxy properties. Measurements of the four strongest Fe II* emission lines are plotted and representative errors are shown in the lower right hand corner. The data points are not independent as there is substantial overlap of objects among the composite spectra. Stronger Fe II* features at 2396 and 2626 Å show kinematics scattering around 0 km s^{-1} while weaker Fe II* lines at 2365 and 2612 Å are on average redshifted by $\sim 100 \text{ km s}^{-1}$. The 2626 Å feature is isolated from neighboring absorption lines and its centroid is therefore the most robust of the Fe II* features. We accordingly conclude that the kinematics of Fe II* emission are consistent with the systemic velocity.

tively, and the reduction procedure – flat-fielding, cosmic ray rejection, background subtraction, one-dimensional extraction, wavelength and flux calibration, and transformation to the vacuum wavelength frame – was completed using IRAF scripts (Martin et al. 2012). The continuum signal-to-noise (S/N) ratios of the LRIS observations over the rest wavelength interval $2400\text{--}2500 \text{ \AA}$ range from $\sim 1\text{--}25 \text{ pixel}^{-1}$ with a median of 6 pixel^{-1} . The average redshift of the sample is $\langle z \rangle = 0.99$ and the full range of redshifts is $0.2 < z < 1.3$.

The spectra were continuum normalized and composite spectra were assembled from stacks of mean-combined rest-frame spectra. No weights were applied in this stacking procedure. Since all data were continuum normalized prior to stacking, this procedure ensures that systems with differing luminosities contribute evenly to the stack and that the stack represents a mean in equivalent width. In assembling the composites, we smoothed the spectra of objects obtained with the 600 line mm^{-1} grism or grating in order to account for the difference in resolution between those obtained with the 600 line mm^{-1} and 400 line mm^{-1} setups. In Figure 1, we show the composite spectrum assembled from all of the data in our sample. Fe II, Mg II, and Mg I resonant absorption lines are significantly detected in the composite spectrum, as are Fe II* and C II] emission lines. Table 1 summarizes the Fe II absorption line and Fe II* emission-line strengths of this composite spectrum.

72 of the galaxies observed with LRIS fall in the Extended Groth Strip and accordingly have extensive multi-wavelength coverage from the All-Wavelength Extended Groth Strip International Survey (AEGIS; Davis et al. 2007). AEGIS observations cover a broad range in wavelength; we utilized *Chandra* X-ray, *Galaxy Evolution Explorer* (GALEX) FUV and NUV imaging, *Hubble Space*

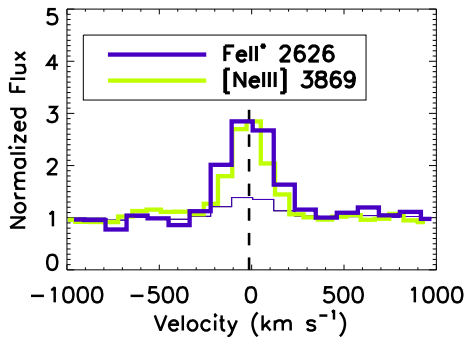


FIG. 4.— Comparison of scaled Fe II* and [Ne III] profiles for a spectral stack of the 12 objects showing $\geq 2\sigma$ detections of Fe II* 2626 Å and $\geq 3\sigma$ detections of the nebular emission line [Ne III] 3869 Å. The unscaled Fe II* profile is shown as a thin line. The kinematics of Fe II* and [Ne III] are similar, with Fe II* showing a velocity offset of -12 km s^{-1} from systemic velocity and [Ne III] shifted by -16 km s^{-1} (overlapping vertical dashed lines). Given the uncertainty on the systemic redshift determination (Section 3), we conclude that the centroids of both the Fe II* 2626 Å and [Ne III] 3869 Å emission lines are consistent with 0 km s^{-1} .

Telescope (*HST*) ACS F606W (*V*) and F814W (*I*) imaging, *BRI* Canada France Hawaii Telescope and Palomar/WIRC *J* and *K_s* imaging, and *Spitzer* IRAC and MIPS pointings in our analyses. We specifically employed *GALEX* observations to estimate dust-corrected SFRs and *HST* imaging to estimate disk inclinations and galaxy areas. We calculated dust-corrected SFRs using UV measurements from *GALEX*, where the dust correction was estimated based on the relationship between the spectral slope β and dust extinction (Seibert et al. 2005). β parameterizes the slope of the flux over the rest-frame interval 1250–2500 Å ($f_\lambda \propto \lambda^\beta$). The inclination of resolved galactic disks was estimated from axis ratios of rest-frame UV imaging, under the assumption that galaxy disks are intrinsically circular. We estimated galaxy areas using a methodology that flags only the brightest star-forming clumps satisfying a threshold star-formation rate surface density. In this paper, we also utilize stellar masses calculated from SED modeling with *BRIK* photometry, assuming Bruzual & Charlot (2003) spectral templates and a (Chabrier 2003) initial mass function. For our study, modeling was done with *BRI* photometry alone if objects lacked *K*-band detections. We refer the reader to Kornei et al. (2012) for a full description of these properties.

3. THE DETERMINATION OF SYSTEMIC AND OUTFLOW VELOCITIES

We discuss our procedure for determining outflow velocities in Martin et al. (2012) and provide here only a summary of the methodology. As the kinematics of galactic winds are only meaningful when compared to a systemic redshift frame, we used nebular emission lines such as [O II] $\lambda\lambda 3726, 3729$, [O III] $\lambda\lambda 4959, 5007$, and the H I Balmer series to define z_{sys} for each galaxy in our sample (Martin et al. 2012). Comparing our measurements of z_{sys} determined from the LRIS data with those given for the DEIMOS data in the DEEP2 catalogs, we find a mean velocity discrepancy of -14 km s^{-1} with a standard deviation of 41 km s^{-1} . We accordingly

assume a conservative systematic redshift uncertainty of 41 km s^{-1} on the systemic redshift measurements and require that secure detections of galactic winds have velocity offsets of at least 41 km s^{-1} .

In Martin et al. (2012), we fit a single-component model simultaneously to five resonant Fe II absorption lines tracing cool ($T < 10^4 \text{ K}$) gas at 2249.88, 2260.78, 2344.21, 2374.46, and 2586.65 Å in the LRIS spectra⁵. The model fit to the Fe II lines has four free parameters: Doppler shift, optical depth at line center, Doppler width (b , where $b = \sqrt{2}\sigma = \text{FWHM}/2\sqrt{\ln 2}$), and covering fraction. Due to the low spectral resolution and finite S/N of the observations, the Doppler shift is the best-constrained parameter and we will not discuss the other three parameters in this paper. We measured velocities for 172/212 objects, where 40 objects had no significant absorption lines and therefore could not be modeled, and find velocities ranging from -302 to $+401 \text{ km s}^{-1}$ with a mean of -30 km s^{-1} and a 1σ sample standard deviation of 89 km s^{-1} . We define here the convention of employing “ V_1 ” to refer to the measured velocity shift of the deepest part of the Fe II absorption line fit, relative to a systemic reference frame typically defined by nebular emission lines. Negative V_1 values refer to blueshifts (“outflows”) while positive V_1 values correspond to redshifts (“inflows”). Fe II velocity shifts significant at the 1σ (3σ) level are observed in $\sim 67\%$ (27%) of the sample. In this paper, we primarily utilize the V_1 measurements of composite spectra due to the high S/N of the composite spectra ($15\text{--}45 \text{ pixel}^{-1}$). We also measured maximal outflow velocities from the blue wing of the 2796 Å Mg II feature (“ $V_{\text{max}}(\text{Mg II})$ ”; Martin et al. 2012). These maximal outflow velocities are not biased by the effects of Mg II emission filling since these measurements are made from the wing of the absorption feature as opposed to the centroid. $V_{\text{max}}(\text{Mg II})$ ranges from -1151 km s^{-1} to a limit of -435 km s^{-1} in 400 line mm^{-1} spectra and -282 km s^{-1} in 600 line mm^{-1} spectra, with the limits set by the resolution of the spectra (Martin et al. 2012).

4. FINE-STRUCTURE FE II* EMISSION

The Fe II ion has many transitions in the rest-frame ultraviolet⁶ and several authors have used Fe II resonant absorption lines to trace the bulk motion of outflowing interstellar gas (Rubin et al. 2010b; Coil et al. 2011; Kornei et al. 2012; Martin et al. 2012). The absorption of a resonant photon can result in either the re-emission of another resonant photon to the ground state (scattering) or the emission of a photon to an excited ground state (fluorescence). We observe resonant Fe II absorption in our data, but do not see resonant Fe II emission. This lack of resonant emission may be due to the limited spectral resolution of our data (FWHM $\sim 435 \text{ km s}^{-1}$), as Erb et al. (2012) observe resonant Fe II emis-

⁵ The Fe II features at 2382.76 and 2600.17 Å are purposefully omitted from fitting as these lines are more susceptible to filling from resonant emission; this “emission filling” can shift the measured centroid of absorption lines to bluer wavelengths (e.g., Prochaska et al. 2011; Martin et al. 2012). We measure Fe II absorption lines as opposed to Mg II absorption lines as the latter suffer more emission filling.

⁶ We refer the reader to Figure 1 of Erb et al. (2012) for an energy level diagram of the Fe II ion.

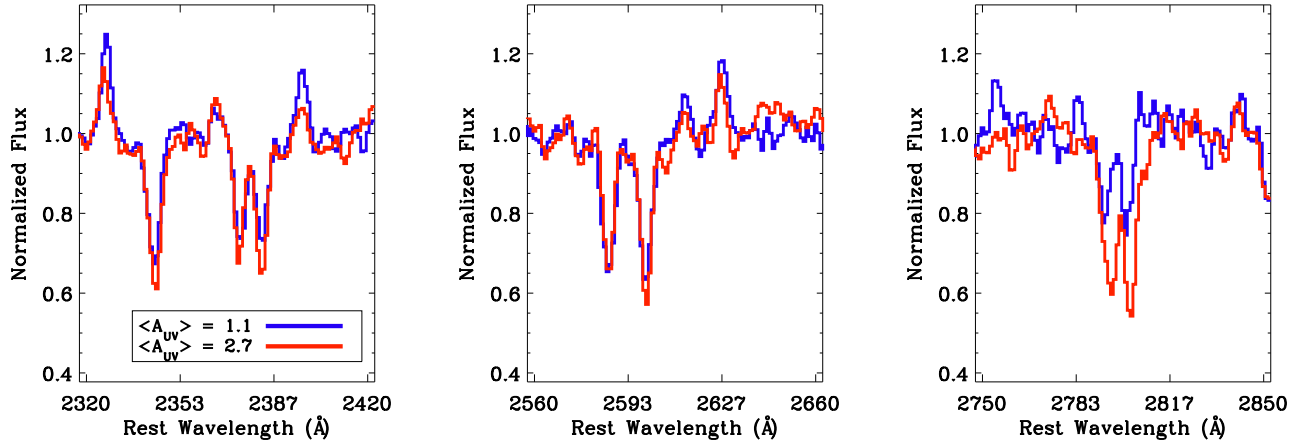


FIG. 5.— A comparison of composite spectra of different dust attenuation levels. Lower attenuation objects ($\langle A_{UV} \rangle = 1.1$) are shown in blue, while higher attenuation objects ($\langle A_{UV} \rangle = 2.7$) are plotted in red. Fe II* emission lines are weaker in dustier systems, consistent with predictions by Prochaska et al. (2011). We find that objects with larger A_{UV} values show, on average, blueshifted 2626 Å Fe II* emission (-20 ± 42 km s $^{-1}$) while objects with lower A_{UV} values exhibit redshifted emission (37 ± 41 km s $^{-1}$). However, the difference between these two values is not statistically different from 0 km s $^{-1}$. We conclude that higher resolution observations are needed in order to test the Prochaska et al. (2011) hypothesis that increased dust attenuation produces more blueshifted Fe II* profiles.

sion at 2600 Å in a subset of their higher resolution data. Here, we focus on the emission features of Fe II resulting from fluorescence. In this work, we examine four Fe II* lines at 2365.55, 2396.35, 2612.65, and 2626.45 Å. An additional Fe II* line within our data’s wavelength coverage, at 2632.11 Å, is absent in individual observations but plausibly detected in a stack of the strongest Fe II*-emitting galaxies.

4.1. Fe II* Emitters and Non-emitters

We measured the equivalent widths of the four strongest Fe II* features for each object in our sample with Fe II* spectral coverage ($> 95\%$ of the sample). The equivalent width of each line was calculated over a fixed wavelength interval approximately 10 Å wide, where the precise wavelength interval was derived from the 3σ extent of each Fe II* feature measured in a high S/N stack of all the spectral data⁷. We find typical rest-frame Fe II* equivalent widths of several tenths of an angstrom, where 23, 37, 23, and 58 objects exhibit $\geq 2\sigma$ detections in each of the four Fe II* lines at 2365, 2396, 2612, and 2626 Å, respectively. We observe that the 2626 Å line is the most frequently detected of the Fe II* lines. Since this feature is relatively isolated from neighboring absorption lines, the kinematics of the 2626 Å line may furthermore be more robust than those of other Fe II* features.

With these measurements of Fe II* equivalent widths, we isolated subsamples of objects exhibiting strong or weak Fe II* emission and examined the structural, outflow, and star-forming properties of these galaxies. We focused our selection criteria on the 2396 Å and 2626 Å features given that the largest number of objects had significant ($\geq 2\sigma$) detections in these lines. Furthermore, a high S/N spectral stack of all the data showed larger equivalent widths for the 2396 and 2626 Å features (0.72

± 0.07 and 0.80 ± 0.09 Å, respectively) than for the 2365 and 2612 Å lines (0.42 ± 0.05 and 0.41 ± 0.09 Å, respectively). None of the Fe II* lines are resolved in either our 400 line mm $^{-1}$ observations or our 600 line mm $^{-1}$ observations.

We define a subsample of 13 “Fe II* emitters” based on objects having $> 4\sigma$ equivalent width detections in either the 2396 Å or 2626 Å lines, where this detection threshold was motivated by visual inspection of objects showing obvious Fe II* emission. We found that selecting objects having $> 3\sigma$ equivalent width detections yielded a sample of 31 objects where several objects showed asymmetric Fe II* profiles that did not appear robust. The 13 objects selected with the $> 4\sigma$ criterion have continuum S/N ranging from 7.8–25.1 pixel $^{-1}$. We also collect a subsample of 9 “Fe II* non-emitters” selected to have $< 1\sigma$ equivalent width detections in both the 2396 Å and 2626 Å lines and continuum S/N > 7.8 pixel $^{-1}$. We imposed a S/N threshold for the Fe II* non-emitter sample in order to ensure a fair comparison with the Fe II* emitter sample. We adopted the simplified methodology of requiring the same S/N threshold for objects observed with either the 400 line mm $^{-1}$ grism or the 600 line mm $^{-1}$ grism. A fixed equivalent width sensitivity will translate to slightly different S/N thresholds depending on the resolution of the data (Martin et al. 2012), so we acknowledge that our technique may be biased toward detecting weaker lines in the higher-resolution 600 line mm $^{-1}$ data. Three of the Fe II* non-emitters have colors typical of “green valley” galaxies (e.g., Martin et al. 2007); our conclusions remain unchanged if these objects are omitted from the sample.

In Figure 2, we compare the composite spectra assembled from the Fe II* emitter and non-emitter samples. The 2365, 2396, 2612, and 2626 Å Fe II* lines are clearly detected in the composite of Fe II* emitters, and the 2632 Å Fe II* line is plausibly seen as a shoulder on the red side of the 2626 Å feature. The relatively low spectral resolution of our data (FWHM ~ 435 km s $^{-1}$) makes it difficult

⁷ The exact wavelength intervals we use are: 2360.4–2371.4 Å for Fe II* 2365 Å, 2390.9–2401.1 Å for Fe II* 2396 Å, 2607.8–2617.2 Å for Fe II* 2612 Å, and 2622.2–2630.3 Å for Fe II* 2626 Å.

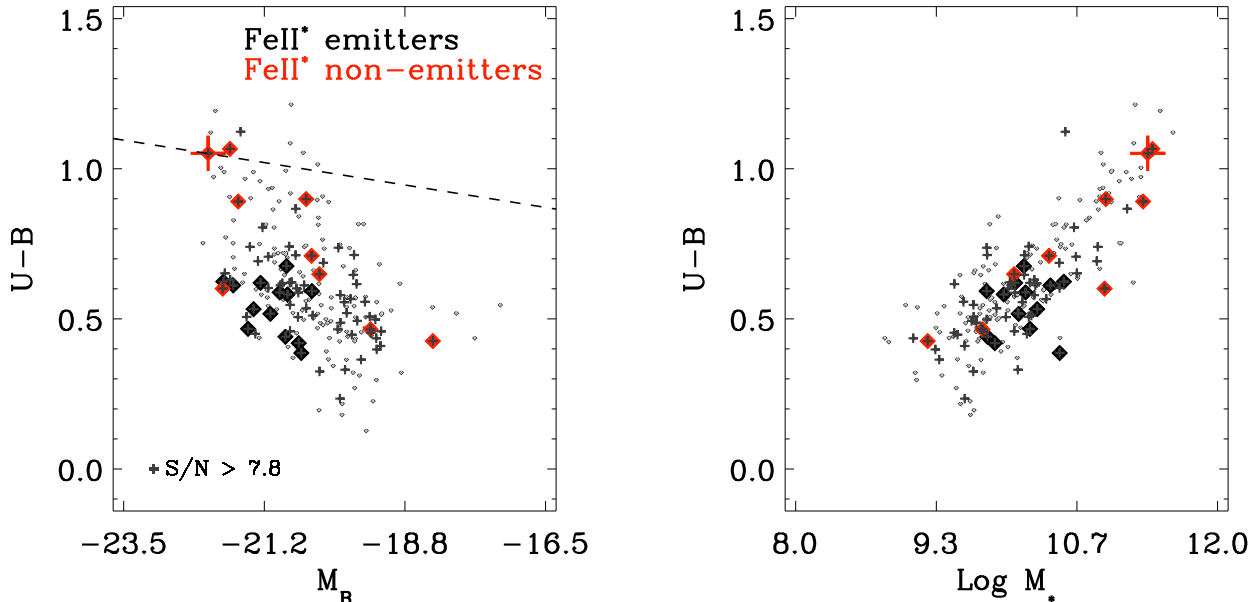


FIG. 6.— Left: color-magnitude diagram of the full sample, where the dashed line indicates the division between red sequence and blue cloud galaxies derived by Willmer et al. (2006). Objects with continuum S/N > 7.8 are indicated with gray crosses. Within this subsample of objects with higher S/N, Fe II* emitters are shown as black diamonds (13 objects) and Fe II* non-emitters are shown as red diamonds (9 objects). Object 12015320, a Fe II* non-emitter, is differentiated with a red cross since it is likely an AGN based on its broad Ne V emission and X-ray flux. Fe II* emitters appear to be preferentially bright, blue galaxies, although Figure 7 shows no statistically significant trend between Fe II* strength and either luminosity or color, based on a binary division of the data. Right: color versus stellar mass plot, where the symbols are the same as in the left panel. Fe II* emitters have lower stellar masses on average than the sample as a whole.

to detect the 2632 Å feature securely given its proximity to the Fe II* line at 2626 Å (-645 km s^{-1}). In a higher-resolution (FWHM $\sim 190 \text{ km s}^{-1}$) composite spectrum of 96 star-forming galaxies at $1 \lesssim z \lesssim 2$, Erb et al. (2012) detect the 2632 Å line at $\sim 4\sigma$ significance and resolve this feature cleanly from the 2626 Å line. The Erb et al. composite spectrum is inclusive of all these authors' data, while the corresponding stack of all of our data does not show any signature of 2632 Å emission; we only observe evidence of 2632 Å emission in the stack of Fe II* emitters. We convolved the Erb et al. spectrum to our lower spectral resolution and found a blended 2626+2632 Å complex consistent with the profile of our data. This similarity in profile shape supports our hypothesis that we detect the 2632 Å line blended with the 2626 Å feature in the stack of Fe II* emitters. We fit two Gaussian profiles simultaneously to our data's 2626+2632 Å complex and find that the strength of 2632 Å emission is approximately half that of the 2612 Å feature, as predicted by the ratio of the Einstein A coefficients of these lines. In the composite spectrum assembled from all of the data in our sample, however, we find that the 3σ upper limit on the strength of 2632 Å emission is 0.21 Å, less than 50% of the strength of the 2612 Å feature (0.55 Å). The relatively low spectral resolution of our data may be responsible for the weaker-than-expected 2632 Å strength.

The composite spectra assembled from the Fe II* emitter and non-emitter samples exhibit different Fe II* strengths, by construction. However, these spectra also show variation in the strength and kinematics of their Fe II and Mg II resonant absorption features. Evidently, the presence or absence of fine-structure Fe II* emission

is linked to the strength and velocity offsets of resonant absorption lines. Based on inspection of the composite spectra assembled from the Fe II* emitter and non-emitter samples, two trends are visually apparent:

1. Fe II* emitters show stronger Fe II resonant absorption lines and weaker Mg II resonant absorption lines than Fe II* non-emitters.
2. Fe II* emitters show more blueshifted Mg II resonant absorption lines than Fe II* non-emitters.

The composite spectrum of Fe II* emitters exhibits a $\sim 50\%$ larger Fe II absorption equivalent width and a $\sim 50\%$ weaker Mg II absorption equivalent width (integrated over both Mg II absorption lines) than the composite spectrum of Fe II* non-emitters. This anticorrelation between Fe II and Mg II absorption strengths is not typical in our sample; composite spectra assembled on the basis of other galaxy properties (Section 4.3) generally show Fe II and Mg II strengths varying in tandem, as Coil et al. (2011) find. Furthermore, the changes in both Fe II and Mg II absorption strength seen in the Fe II* emitter and non-emitter composite spectra are not as large as the changes observed in other composite spectra. As we show later, Fe II* emitters are preferentially at larger redshifts than Fe II* non-emitters. We propose that the redshift difference between Fe II* emitters and non-emitters may be responsible for some of the trends we observe in Figure 2, as we discuss both in this section and later in the paper. In order to control against redshift evolution, we would ideally assemble a sample in which Fe II* emitters and non-emitters are at similar redshifts. Future studies with more objects in each redshift bin will be instrumental in examining the properties of Fe II* emitters and non-emitters independent of

potential biases caused by redshift evolution.

We explore the relationship between Fe II* emission and Fe II absorption more thoroughly in Martin et al. (in preparation) but note here that our finding of stronger Fe II absorption in the Fe II* emitter sample is contrary to the trends observed in most of the other composite spectra presented in this paper (Section 4.3). The majority of the composite spectra exhibit weaker Fe II absorption paired with stronger Fe II* emission, while Figure 2 instead shows stronger Fe II absorption with stronger Fe II* emission. This observation that stronger Fe II absorption accompanies stronger Fe II* emission is furthermore inconsistent with the results of Erb et al. (2012). These authors examined 96 star-forming galaxies at $1 \lesssim z \lesssim 2$ and found a trend of decreasing Fe II* emission with increasing Fe II absorption. Erb et al. suggest that systems with stronger Fe II absorption may be preferentially dusty and therefore show only weak Fe II* emission. Erb et al. also propose that galaxy inclination modulates the observed ratio of emission and absorption equivalent widths, as an anisotropic (i.e., biconical) outflow will exhibit differing ratios of emission and absorption depending on viewing angle: a biconical wind viewed edge-on will show more emission than absorption while a face-on view of the same galactic wind will show more absorption than emission. These predictions make sense given that a wind seen face-on (down the barrel) shows material absorbed against the background light of the host galaxy while observations of a wind edge-on see the wind projected 90° and therefore record more scattered emission as opposed to absorption backlit by starlight. Furthermore, Erb et al. suggest that slit losses – arising because the size of the Fe II*-emitting region is larger than the area encompassed by the spectroscopic slit – may reduce the observed strength of Fe II* emission in galaxies subtending larger angular sizes. In $z \sim 3$ Lyman break galaxies, Shapley et al. (2003) found that Si II* emission lines were much weaker than the Si II resonant absorption lines. These authors hypothesized that the narrow spectroscopic slit ($1.''4$) might be subtending only a small fraction of the area in which Si II* emission was arising. Steidel et al. (2010) showed that interstellar absorption persists at distances of several tens of kpc from galaxies; emission lines arising from similar galactocentric distances would fall beyond the extent of most spectroscopic slits. Findings by Jones et al. (2012) also support the hypothesis that fine-structure emission may be spatially extended. These authors used a sample of 81 Lyman break galaxies at $z \sim 4$ and found that objects had average Si II*/Si II equivalent width ratios of ~ 0.5 , indicative of a loss of fine-structure photons. As the galaxies examined by Jones et al. (2012) suffer only minimal dust attenuation ($E(B-V) \sim 0.10$), this discrepancy in equivalent width is likely due to fine-structure emission being more spatially extended than resonant emission as opposed to emission being suppressed by dust. Jones et al. (2012) also infer a change in the spatial extent of Si II* emission between $z \sim 3$ and $z \sim 4$ based on the different Si II*/Si II equivalent width ratios seen in their data and a $z \sim 3$ Lyman break galaxy sample (Shapley et al. 2003). As objects at $z \sim 4$ show a larger average Si II*/Si II equivalent width ratio (~ 0.5) than objects at $z \sim 3$ (~ 0.2), Jones et al. (2012) suggest that the characteristic size of the Si II*-emitting region

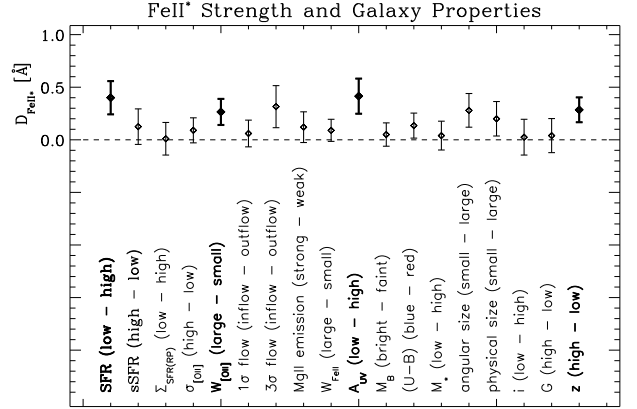


FIG. 7.— Variation of Fe II* emission strength with galaxy properties. D_{FeII^*} , a parameterization of how Fe II* strength changes between two spectra (Section 4.3), is shown for pairs of composite spectra assembled according to 18 different galaxy properties. The largest D_{FeII^*} values, significant at $> 2\sigma$, are observed for three galaxy properties: SFR, A_{UV} , and $W_{[\text{OIII}]}$, as well as z (bold text). Stronger Fe II* emission is seen for lower SFR, larger $W_{[\text{OIII}]}$, lower A_{UV} , and higher z objects. D_{FeII^*} values are significant at $> 1\sigma$ for the following additional parameters: 3σ gas flow, $U - B$ color, angular size, and physical size, such that Fe II* emission is more pronounced in systems with 3σ inflows (as opposed to 3σ outflows), bluer $U - B$ colors, smaller angular sizes, and smaller physical sizes. Our finding that objects with smaller angular sizes show stronger Fe II* emission is consistent with the hypothesis that slit losses modulate Fe II* emission strength.

decreases from $z \sim 3$ to $z \sim 4$. A similar redshift dependency of the Fe II*/Fe II equivalent width ratio is not observed, however, between our current data set ($\langle z \rangle = 1.0$) and the Erb et al. (2012) sample ($\langle z \rangle = 1.6$); the composite spectra of both studies show Fe II*/Fe II equivalent width ratios of $\sim 0.3 \pm 0.02$. Since the slit widths employed in both studies are comparable and the difference in angular diameter distance at the average redshift of each sample is only $\sim 6\%$, we conclude that the size of the Fe II*-emitting region does not evolve substantially in the 1.8 Gyr intervening between $z \sim 1$ and $z \sim 1.6$.

Fe II* emitters are marked by stronger Fe II absorption, and weaker Mg II absorption, than Fe II* non-emitters. These spectral results are surprising given that the majority of composite spectra used in our study show Fe II and Mg II strengths varying together. Furthermore, most composites that show stronger Fe II* emission also exhibit comparable, or weaker, Fe II absorption (Section 4.3). We propose that the weaker Mg II absorption seen in the composite spectrum of Fe II* emitters is primarily caused by Mg II emission filling. Emission filling is a likely explanation given that Fe II* emitters are bluer than Fe II* non-emitters (Section 4.3) and therefore suffer less dust attenuation. Furthermore, the composite spectrum of Fe II* emitters shows emission redwards of the Mg II 2803 Å absorption feature; that this emission is present supports the theory of emission filling. Additionally, the kinematic shifts observed in the Mg II profiles of the Fe II* emitter and non-emitter composites are consistent with the effects of emission filling. Fe II* emitters show, on average, significantly blueshifted Mg II absorption, as expected from emission filling (e.g., Prochaska et al. 2011; Martin et al. 2012). The centroids of both features of the Mg II doublet are blueshifted in

TABLE 1
 FE II AND FE II* LINES IN THE GLOBAL COMPOSITE SPECTRUM

λ^a (Å)	J_{lower}^b	J_{upper}^b	A_{21}^c (s^{-1})	Feature Type	Equivalent Width ^d (Å)
2344.21	9/2	7/2	1.7×10^8	resonant abs.	1.94 ± 0.06
2365.55	7/2	7/2	5.9×10^7	fine-structure em.	-0.42 ± 0.05
2380.76	5/2	7/2	3.1×10^7	fine-structure em.	... ^e
2374.46	9/2	9/2	4.3×10^7	resonant abs.	1.39 ± 0.08
2396.35	7/2	9/2	2.6×10^8	fine-structure em.	-0.72 ± 0.07
2382.77	9/2	11/2	3.1×10^8	resonant abs.	$1.53^e \pm 0.06$
2586.65	9/2	7/2	9.0×10^7	resonant abs.	1.72 ± 0.06
2612.65	7/2	7/2	1.2×10^8	fine-structure em.	-0.41 ± 0.09
2632.11	5/2	7/2	6.3×10^7	fine-structure em.	-0.21^f
2600.17	9/2	9/2	2.4×10^8	resonant abs.	2.35 ± 0.09
2626.45	7/2	9/2	3.5×10^7	fine-structure em.	-0.80 ± 0.09

^a Vacuum wavelengths from Ralchenko et al. (2005).

^b Orbital angular momenta.

^c Einstein A coefficients.

^d Equivalent width of feature measured in the global composite spectrum (Figure 1).

Negative equivalent widths correspond to features in emission.

^e Fe II* 2380.76 Å is blended with Fe II 2382.77 Å.

^f 3σ upper limit.

the Fe II* emitter composite relative to the Fe II* non-emitter composite. The Fe II* emitter composite has Mg II lines with centroids of $-319 \pm 28 \text{ km s}^{-1}$ and $-247 \pm 46 \text{ km s}^{-1}$ for the 2796 and 2803 Å features, respectively. The Fe II absorption lines are not significantly blueshifted in the Fe II* emitter spectrum. The Mg II doublet is optically thick at lower column densities than the majority of the Fe II transitions studied here. Mg II is therefore a better probe of rarefied gas, which may have a high-velocity component (Martin et al. 2012). The Fe II* non-emitter composite has Mg II centroids of $0 \pm 65 \text{ km s}^{-1}$ and $-58 \pm 44 \text{ km s}^{-1}$, respectively. These results suggest that the conditions enabling observations of high-velocity Mg II gas may be the same conditions conducive to seeing Fe II* emission. This hypothesis is consistent with predictions by Prochaska et al. (2011) that stronger Fe II* emission is seen when viewing a galactic wind face-on (i.e., in conditions favorable for detecting blueshifted absorption lines; Kornei et al. 2012), but contradictory with the interpretation from Erb et al. (2012) that a galactic wind seen face-on will show more absorption than emission.

While emission filling may be responsible for shifting the centroids of Mg II, we also observe that the blue wings of the Mg II doublets are offset between the Fe II* emitter and non-emitter composite spectra. The different velocities seen in the blue wings of the features – where emission filling is negligible – indicate an intrinsic discrepancy in the observed Mg II gas kinematics between the Fe II* emitter and non-emitter populations. However, the $V_{\text{max}}(\text{Mg II})$ values for the Fe II* emitter and non-emitter composite spectra are consistent within their errors given the similar line profiles of the composite spectra where $V_{\text{max}}(\text{Mg II})$ is measured; we emphasize the overall difference in the line profiles here as opposed to relying on the single parametrization of $V_{\text{max}}(\text{Mg II})$. The distinct blue wing profiles of the Fe II* emitter

and non-emitter composite spectra suggest that the line profiles differ more substantially than can be explained solely by emission filling.

Although these composite spectra show a direct link between Mg II gas kinematics and the strength of Fe II* emission lines such that galaxies with blueshifted Mg II absorption lines are more likely to have stronger Fe II* emission, not all of our findings are consistent with the trend that observations of gas flows are most often observed when stronger Fe II* emission is observed. We assembled composite spectra on the basis of both V_1 and $V_{\text{max}}(\text{Mg II})$ and found no statistically significant difference in Fe II* strength when the data were divided by gas flow velocity. Furthermore, we examined distributions of V_1 and $V_{\text{max}}(\text{Mg II})$ and found no evidence that objects with either strong or weak Fe II* emission were clustered in velocity space.

Modeling of galactic winds is important for understanding the link between the observability of Fe II* emission and the frequency of observed prevalence of gas flows. In particular, models of biconical galactic winds – a geometry prevalent in both local and $z \sim 1$ samples (e.g., Heckman et al. 1990; Martin et al. 2012) – will be critical to investigating how the measured frequency of fine-structure emission varies as a function of observed gas flow properties. Prochaska et al. (2011) studied the prevalence of emission in a model of a hemispherical wind, but thus far accurate modeling of more collimated outflows observed at different viewing angles has been lacking from the literature.

4.2. Fe II* Kinematics

While blueshifted or redshifted Fe II* emission is consistent with moving gas, Prochaska et al. (2011) showed that emission profiles arising in the presence of gas flows can still be centered at roughly 0 km s^{-1} . Therefore, the absence of a net kinematic offset does not necessar-

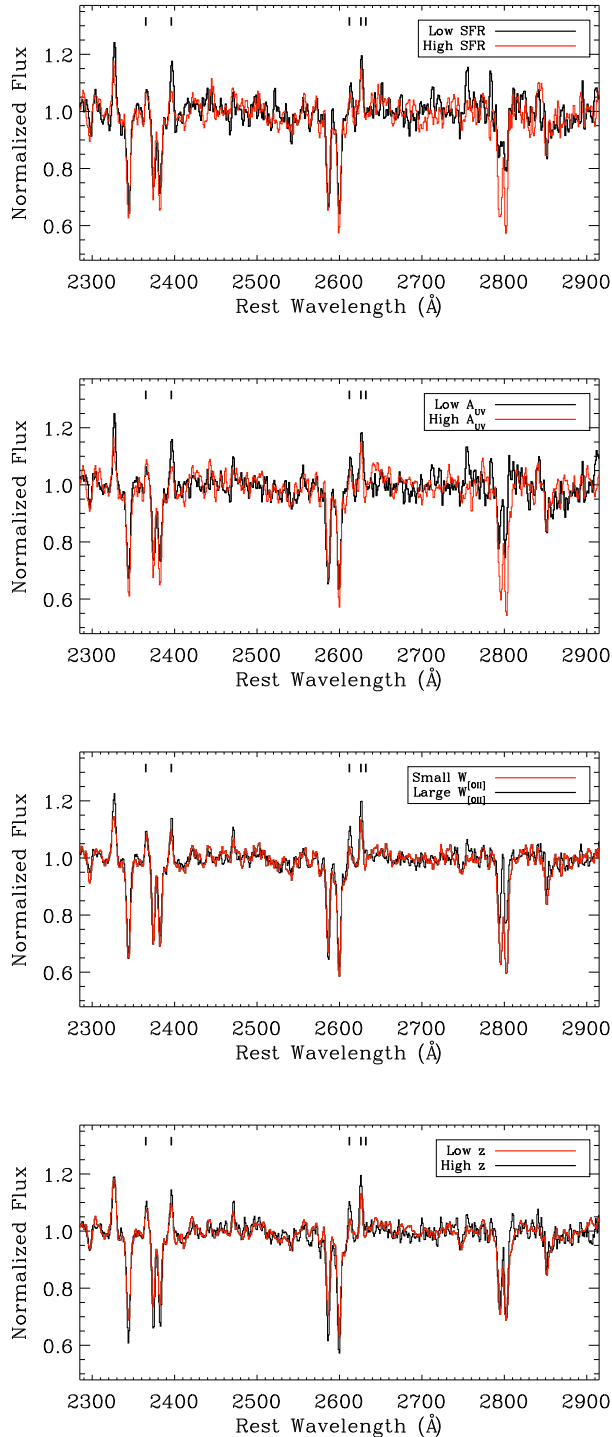


FIG. 8.— Composite spectra of galaxy parameters that strongly modulate Fe II* emission strength. From top to bottom, composite spectra are shown comparing low and high SFR, low and high A_{UV} , small and large $W_{[OII]}$, and low and high z . In each case, the composite spectrum with stronger Fe II* emission is plotted in black. The composite spectra have $S/N \sim 30 \text{ pixel}^{-1}$.

ily imply that the associated gas is at rest with respect to a galaxy’s stars. We measured the centroids of the Fe II* lines in the Fe II* emitter composite spectrum using Gaussian fits from the IDL routine `gaussfit`. We find that the 2365, 2396, 2612, and 2626 Å lines have centroids of -40 ± 111 , -36 ± 28 , 7 ± 33 , and $-6 \pm 21 \text{ km s}^{-1}$, respectively, where errors were estimated from Monte Carlo simulations. The large uncertainty on the centroid of the 2365 Å line is due to the low equivalent width of this line. We conclude that the Fe II* centroids are consistent with the systemic velocity, given both the measured uncertainties on the velocities and the uncertainty on the systemic redshift determination (Section 2). These measurements are accordingly consistent with Fe II ions tracing either gas flows or stationary H II regions. In a sample of star-forming galaxies at $1 \lesssim z \lesssim 2$, Erb et al. (2012) found that $[O II]/Fe II^*$ line ratios were too large to be consistent with simple photoionization models. These authors suggest that Fe II* emission arises from photon scattering in the galactic outflow.

We also measured the centroids of the Fe II* lines in other composite spectra assembled on the basis of an array of morphological (e.g., size) and stellar population (e.g., SFR) parameters and we show the results in Figure 3. In the ensemble of composite spectra, which are not independent due to substantial overlap of objects among the composites, we find that the strongest Fe II* lines at 2396 and 2626 Å have centroids scattering around 0 km s^{-1} while the weaker Fe II* lines at 2365 and 2612 Å are predominantly redshifted. All of the Fe II* lines of all of the composite spectra are within 3σ of 0 km s^{-1} , however, with the sole exception of one line (the 2365 Å centroid of the composite spectrum assembled from objects with large angular sizes). We propose that the systematic redshift observed in the 2365 and 2612 Å line centroids are due to the weaker strength of these lines relative to the other Fe II* features and the proximity of these lines to Fe II absorption features. Since all the Fe II* emission lines trace the same underlying population of gas, we conclude that the kinematics of Fe II* emission are consistent with 0 km s^{-1} based on the measurements of the strongest Fe II* features. Given the relatively low S/N of our data, it is difficult to robustly measure the kinematics of Fe II* emission in individual objects.

A complementary investigation of Fe II* kinematics is to compare the velocity offsets of a strong Fe II* line and a nebular emission line (e.g., Rubin et al. 2011). Nebular emission lines such as $[Ne III]$ trace star-forming regions and therefore probe stationary gas. In Figure 4, we show the Fe II* 2626 Å and $[Ne III]$ 3869 Å features of a composite spectrum assembled from the spectra of 12 objects with strong detections of both Fe II* 2626 Å and $[Ne III]$ 3869 Å. The kinematics of these two lines are similar; the Fe II* line has a centroid of -12 km s^{-1} while the $[Ne III]$ line has a centroid of -16 km s^{-1} . In light of the uncertainty on our determination of the systemic redshift, we conclude that both Fe II* and $[Ne III]$ have kinematics consistent with being centered at 0 km s^{-1} .

Rubin et al. (2011) measured the kinematics of Fe II* lines in the spectrum of a starburst galaxy at $z \sim 0.69$ and found that Fe II* lines trace gas that is redward

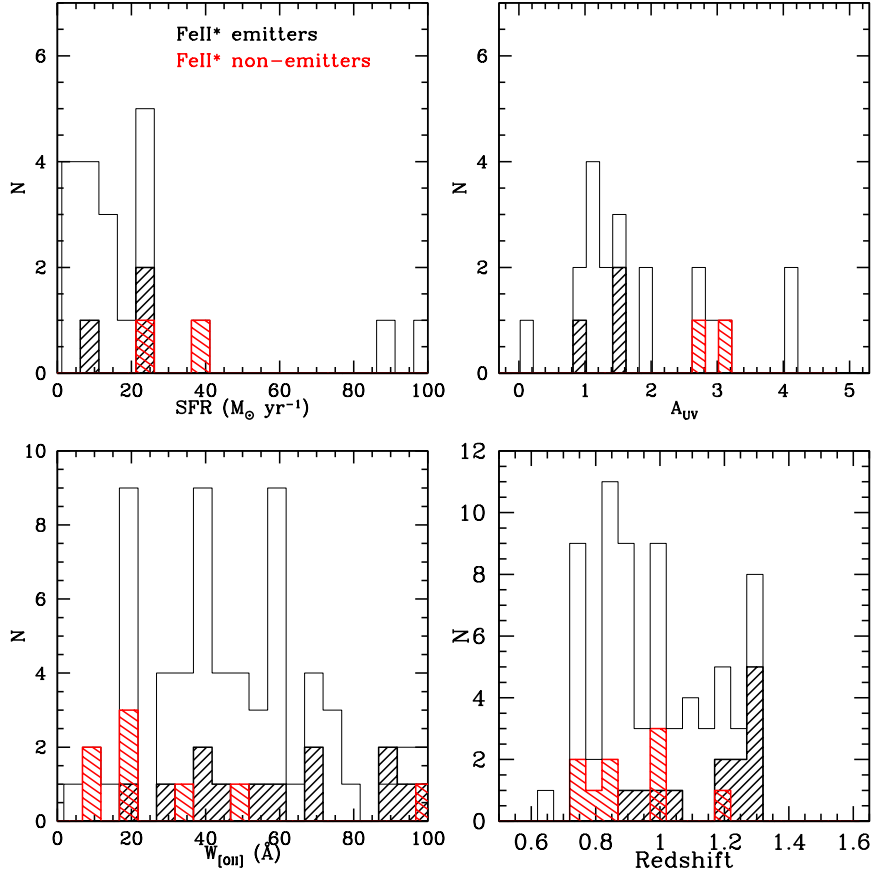


FIG. 9.— Histograms of the four parameters most strongly modifying Fe II* emission strength: SFR, A_{UV} , $W_{[OII]}$, and z . In each panel, the open histogram shows the parent sample of objects with $S/N > 7.8$. Fe II* emitters are shown in the black shaded histogram and Fe II* non-emitters are indicated with the red shaded histogram. Fe II* emitters are characterized on average by smaller SFRs, lower dust attenuations, larger $W_{[OII]}$, and larger redshifts than Fe II* non-emitters.

or within 30 km s^{-1} of the systemic velocity. These authors note that the kinematics of Fe II* features are inconsistent with the kinematics of both FeII resonant absorption lines ($\Delta V \sim -200 \text{ km s}^{-1}$, where ΔV is the offset from systemic velocity) and features tracing galactic H II regions ($[\text{NeIII}]$, $\text{H}\delta$, $\text{H}\gamma$; $\Delta V \sim 0 \text{ km s}^{-1}$). Consistent with Rubin et al. (2011), Coil et al. (2011) found that Fe II* lines are typically within 2σ of the systemic redshift in a sample of post-starburst and AGN host galaxies at $0.2 < z < 0.8$. These authors propose that Fe II* emission arises in galactic winds as opposed to star-forming regions, since Fe II* emission is observed in post-starburst galaxies not currently experiencing star formation. In composite spectra of star-forming galaxies at $1 \lesssim z \lesssim 2$, Erb et al. (2012) find that Fe II* 2626 Å exhibits blueshifted velocity centroids of about -50 km s^{-1} , although these authors report that individual spectra show Fe II* 2626 Å centroids scattering around 0 km s^{-1} . Erb et al. conclude that Fe II* 2626 Å is on average observed at velocities closer to systemic than the resonant Fe II absorption lines. While the high S/N composite spectra of Erb et al. show Fe II* kinematics near the systemic velocity, as we find in our own sample, higher resolution observations of a larger number of individual objects are needed in order to definitively measure the kinematics of fine-structure emission lines

on a per-object basis. The composite spectra used here for measuring Fe II* kinematics have significantly higher S/N ($15\text{--}45 \text{ pixel}^{-1}$) but lower resolution ($\text{FWHM} \sim 435 \text{ km s}^{-1}$) than the spectra of individual objects employed by both Rubin et al. (2011) and Coil et al. (2011). Our data also have higher S/N than the composite spectra employed by Erb et al. (2012), although our observations are lower resolution than the Erb et al. (2012) data ($\text{FWHM} \sim 190 \text{ km s}^{-1}$).

Numerous studies have developed models of line emission associated with galactic winds (e.g., Verhamme et al. 2006; Steidel et al. 2010; Rubin et al. 2011; Prochaska et al. 2011). In particular, Prochaska et al. (2011) present modeling of Fe II* emission arising from photons scattered in galactic winds. These authors predict Fe II* emission at velocities close to the systemic velocity, since an optically thin galaxy will transmit the Fe II* emission scattered from both the backside and frontside of the wind. However, Prochaska et al. (2011) also note that increased dust opacity may produce more blueshifted Fe II* profiles as the redshifted photons scattering off the backside of the wind will be preferentially absorbed by dust due to their longer path lengths. In Figure 5, we compare composite spectra assembled on the basis of A_{UV} . While we find that objects with larger A_{UV} values show, on

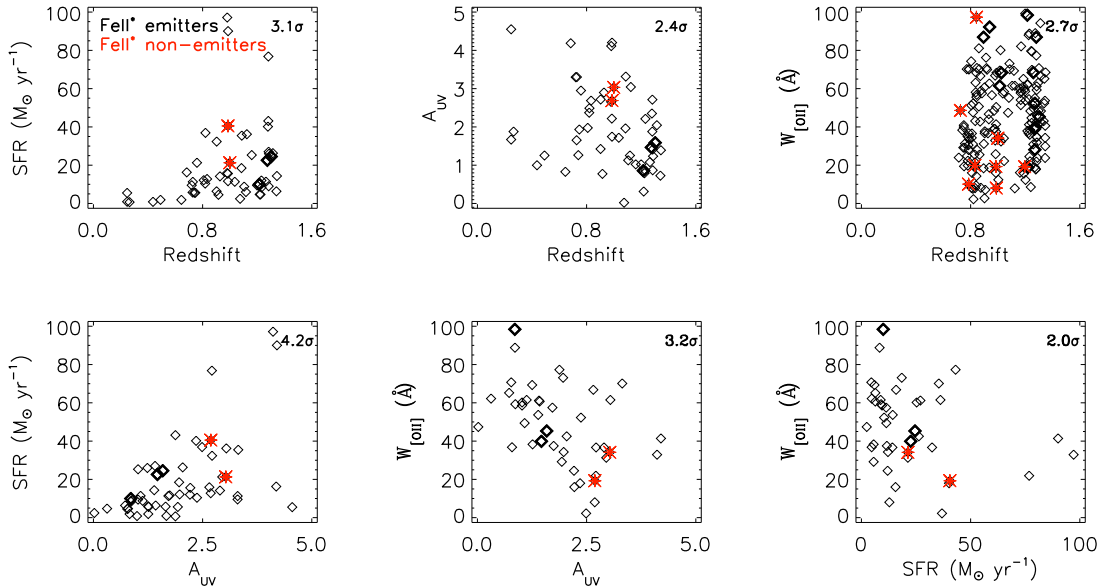


FIG. 10.— Top panels: SFR, A_{UV} , and $W_{[OII]}$ (from left to right) versus redshift, where Fe II* emitters are indicated with thick black diamonds and Fe II* non-emitters are shown as red stars. Higher redshift objects have lower A_{UV} values, on average, than objects at lower redshifts; this trend favors galaxies at higher redshifts exhibiting stronger Fe II* emission than lower-redshift galaxies. Bottom panels: correlations among A_{UV} , SFR, and $W_{[OII]}$, using the same notation as above. SFR and A_{UV} are positively correlated, while both $W_{[OII]}$ and A_{UV} and $W_{[OII]}$ and SFR are inversely correlated. These correlations are consistent with A_{UV} being the primary modulator of Fe II* emission, given that Fe II* emitters are characterized by smaller SFRs and larger $W_{[OII]}$ values than Fe II* non-emitters.

average, more blueshifted 2626 Å Fe II* emission (-20 ± 42 km s $^{-1}$) than objects with smaller A_{UV} values (37 ± 41 km s $^{-1}$), the kinematic differences are small and not statistically significant given the systematic uncertainties in systemic redshift of our data. We note that the C II] emission line at 2326 Å is more blueshifted in objects with larger A_{UV} values, but as this feature is a blend of several C II] lines the precise rest-frame centroid of this line is uncertain. Higher resolution data are needed in order to test the hypothesis of Prochaska et al. (2011) that increased dust attenuation produces more blueshifted emission line profiles.

4.3. Fe II* Emission Strength and Galaxy Properties

In light of the diversity of Fe II* emission strengths observed in our sample, it is important to determine which galaxy properties modulate Fe II* emission. Figure 6 shows a color-magnitude diagram with the 13 Fe II* emitters and 9 Fe II* non-emitters highlighted. Objects showing strong Fe II* emission are brighter ($\langle M_B \rangle = -21.0 \pm 0.1$), bluer ($\langle U - B \rangle = 0.54 \pm 0.02$), and lower stellar mass ($M_* = 1.6 \pm 0.2 \times 10^{10} M_\odot$) than both Fe II* non-emitters ($\langle M_B \rangle = -20.7 \pm 0.4$, $\langle U - B \rangle = 0.75 \pm 0.07$, $\langle M_\odot \rangle = 9.7 \pm 3.1 \times 10^{10} M_\odot$) and the global sample of objects with comparable S/N in their LRIS spectra ($\langle M_B \rangle = -20.5 \pm 0.1$, $\langle U - B \rangle = 0.59 \pm 0.02$, $\langle M_\odot \rangle = 2.8 \pm 0.5 \times 10^{10} M_\odot$). This result is consistent with the interpretation by Prochaska et al. (2011) and Erb et al. (2012) that Fe II* emitters likely have little dust attenuation. Below, we use our extensive multi-wavelength data set to investigate how Fe II* strength depends on a variety of galaxy properties.

We measured the strength of Fe II* emission in 18 pairs of composite spectra assembled based on star-forming,

gas flow, interstellar gas (i.e., Fe II and Mg II), stellar population, size, morphological, and redshift parameters. The star-forming properties include SFR, specific SFR (sSFR = SFR/stellar mass), SFR surface density assuming a Petrosian galaxy area ($\Sigma_{SFR}(RP)$), [O II] emission linewidth corrected for instrumental resolution ($\sigma_{[OII]}$), and [O II] emission line equivalent width ($W_{[OII]}$). The gas flow properties are described by the presence of outflows or inflows detected at or above the 1σ or 3σ levels. Interstellar gas properties include the presence of Mg II emission and the Fe II 2344 Å absorption equivalent width (W_{FeII}). Dust attenuation (A_{UV}), B -band luminosity (M_B), $U - B$ color, and stellar mass (M_*) are the measured stellar population parameters. Size and morphological properties include angular size, physical size, disk inclination (i), and Gini coefficient (G ; Lotz et al. 2004). Redshift, measured spectroscopically, is an additional parameter. We summarize the composite spectra used in this paper in Table 2.

For each property, we assembled composite spectra based on a binary division of the data according to that parameter (i.e., low SFR and high SFR, etc.). Fe II* emission is prominent in all the composite spectra, although its strength varies as a function of galaxy properties. We investigated how the strength of Fe II* changed between each pair of composite spectra using equivalent width measurements of the strongest Fe II* features at 2396 and 2626 Å. We measured local continua around each Fe II* line and defined the extent of each feature as the region where the flux was greater than the continuum. A Gaussian profile was fit to each Fe II* line and an equivalent width was estimated by integrating the Gaussian fit and dividing the summed flux by the local continuum. We define the quantity D_{FeII*} as the average of the equivalent width differences between each

pair of composite spectra:

$$D_{\text{FeII}^*} = \frac{\Delta\text{EW}_{2396} + \Delta\text{EW}_{2626}}{2} \quad (1)$$

where ΔEW_{2396} is the difference in Fe II* 2396 Å equivalent widths between the composite spectra and ΔEW_{2626} is the analogous difference for the 2626 Å line. D_{FeII^*} accordingly has units of Å. In Figure 7, we show the values of D_{FeII^*} for the 18 parameters. We observe D_{FeII^*} ranging from 0.0–0.4 Å. The uncertainty on D_{FeII^*} , δD_{FeII^*} , was estimated through Monte Carlo realizations: for each composite spectrum, we constructed 1000 simulated spectra by perturbing the data at each wavelength by a value drawn from a Gaussian distribution of 1σ width equal to the data’s error spectrum at that wavelength. We measured the Fe II* equivalent widths for each ensemble of 1000 simulated spectra and adopted the standard deviation of the equivalent width distribution as the error. We estimated δD_{FeII^*} for each parameter by propagating errors through Equation 1. The average δD_{FeII^*} of the sample is 0.15 Å and δD_{FeII^*} ranges from 0.11–0.20 Å.

D_{FeII^*} is significant at $\geq 2\sigma$ for four parameters: z , SFR, A_{UV} , and $W_{[\text{OII}]}$. Stronger Fe II* emission is seen in higher redshift objects, those with lower SFRs, lower A_{UV} values, and larger $W_{[\text{OII}]}$ measurements. Erb et al. (2012) also find stronger Fe II* emission in objects with lower SFRs; their analyses on the basis of A_{UV} were inconclusive and these authors do not assemble composite spectra according to $W_{[\text{OII}]}$ or redshift. In Figure 8, we show the four pairs of z , SFR, A_{UV} , and $W_{[\text{OII}]}$ composite spectra. It is important to highlight that the composite spectra assembled on the basis of SFR, A_{UV} , and $W_{[\text{OII}]}$ exhibit different properties from those in the composite spectra assembled according to z . The stronger Fe II* emission observed in the lower SFR, lower A_{UV} , and larger $W_{[\text{OII}]}$ composite spectra is accompanied by weaker Mg II absorption and similar, if not weaker, Fe II absorption. However, the higher z composite shows stronger Fe II* emission and yet comparable Mg II absorption and stronger Fe II absorption than the lower z composite; these spectral trends echo those seen in the composite spectra divided according to Fe II* emission strength (Figure 2). It appears that the division of objects on the basis of redshift yields significantly different spectral trends from those based on the division of the sample according to SFR, A_{UV} , or $W_{[\text{OII}]}$. We propose that the different redshift distributions of Fe II* emitters and non-emitters – where emitters are preferentially at higher redshift – and the changing make-up of our sample properties with redshift contribute to the trends seen in the composite spectra assembled in bins by redshift, since objects in the DEEP2 survey at higher redshifts are preferentially bluer. In summary, Fe II* emission strength increases at higher redshifts, in contrast to the lack of evolution in the Fe II*/Fe II equivalent width ratio described in Section 4.1. We attribute this evolution in Fe II* emission strength to changes in global galaxy properties with redshift.

While the above analyses relied on a binary division of the data according to galaxy properties, we also employed a complementary investigation of the links be-

tween Fe II* emission and z , SFR, A_{UV} , and $W_{[\text{OII}]}$. Specifically, we utilized our samples of Fe II* emitters and non-emitters (Section 4.1) to study if and how these two samples separate in z , SFR, A_{UV} , and $W_{[\text{OII}]}$ parameter space (Figure 9). Each of these four parameters shows a separation of Fe II* emitters and non-emitters, although the sample size is small in the cases of SFR and A_{UV} . The larger sample of objects with redshifts and $W_{[\text{OII}]}$ measurements permits a Kolmogorov-Smirnov (KS) test of the probability that emitters and non-emitters are drawn from the same parent population. We find a probability of 0.003 that the redshifts of the Fe II* emitters and non-emitters arise from the same distribution and a 0.03 probability that the $W_{[\text{OII}]}$ values of the emitters and non-emitters are from the same parent population. While this result indicates in particular the high significance with which Fe II* emitters and non-emitters separate in redshift space, such that Fe II* emitters are preferentially found at larger redshifts, z is not an intrinsic property of a galaxy. It is therefore important to examine how SFR, A_{UV} , and $W_{[\text{OII}]}$ themselves are correlated with z in order to investigate if the observed trend between Fe II* emission strength and z is only a secondary correlation or a function of redshift correlating with intrinsic galaxy properties.

In Figure 10, we show how SFR, A_{UV} , and $W_{[\text{OII}]}$ are themselves interrelated: systems with larger SFRs have larger A_{UV} values, systems with stronger $W_{[\text{OII}]}$ have lower A_{UV} values, and systems with stronger $W_{[\text{OII}]}$ have lower SFRs. SFR, A_{UV} , and $W_{[\text{OII}]}$ are accordingly correlated such that the stronger Fe II* emission in objects with lower SFRs, lower A_{UV} values, and larger $W_{[\text{OII}]}$ measurements can be explained as arising primarily due to the effect of a single parameter: A_{UV} . Furthermore, the correlation between redshift and A_{UV} is likely responsible for the observed correlation between Fe II* emission strength and z . Figure 10 also shows the correlations of SFR, A_{UV} , and $W_{[\text{OII}]}$ versus redshift. Redshift and SFR are correlated at the 3.1σ level ($r_S = 0.44$, where r_S is the Spearman rank-order correlation coefficient) and higher redshift systems have higher SFRs. This positive correlation between redshift and SFR is in the opposite sense of the trends we find with Fe II* emission strength, where both low-SFR and high-redshift systems show stronger Fe II* emission. We find a correlation at the 2.4σ level ($r_S = -0.33$) between redshift and A_{UV} , such that higher redshift systems are less attenuated. That higher redshift objects have both higher SFR and lower A_{UV} appears at first contradictory, given that SFR and A_{UV} are themselves positively correlated at a given redshift (this work; Brinchmann et al. 2004). These trends can be explained by the results of Adelberger & Steidel (2000), where these authors noted that at a given SFR, objects at higher redshifts are less attenuated than their lower-redshift counterparts. Additionally, the R -band selection limits of the DEEP2 survey dictate that objects at higher redshifts must be either brighter or bluer to still fall in the selection window. Therefore, it would be expected that objects at higher redshifts are preferentially bluer than lower-redshift galaxies. Finally, we find a 2.7σ correlation ($r_S = 0.20$) between redshift and $W_{[\text{OII}]}$, in the sense that higher-redshift objects have larger $W_{[\text{OII}]}$ measurements. The correlation between redshift and A_{UV} is sug-

gestive that the trend between redshift and Fe II* arises simply as a secondary correlation and that A_{UV} is the primary property modulating Fe II* emission strength (Section 6.1). Furthermore, the correlation observed between A_{UV} and Fe II* emission strength cannot simply be an artifact of the manner in which A_{UV} is estimated and Fe II* emission equivalent width measured, even though both quantities depend on the properties of the UV continuum. Given that galaxies with lower A_{UV} values have slightly higher UV continuum luminosity densities on average than those with higher A_{UV} values, one expects a *lower* Fe II* emission equivalent width at lower A_{UV} for a fixed Fe II* emission-line flux (contrary to what we observe).

Other parameters besides SFR, A_{UV} , $W_{[OII]}$, and z may modulate Fe II* emission strength. We find that 3σ gas flow, $U - B$ color, the presence of Mg II emission, angular size, and physical size have D_{FeII^*} values significant at $\geq 1\sigma$, such that stronger Fe II* emission is seen in systems with 3σ inflows (as opposed to 3σ outflows), bluer $U - B$ colors, stronger Mg II emission, smaller angular sizes, and smaller physical sizes. The stronger Fe II* emission observed in systems with smaller angular sizes is consistent with the theory that slit losses may be responsible for the lack of Fe II* emission in local galaxy samples (e.g., Giavalisco et al. 2011; Erb et al. 2012). Curiously, we do not find a significant correlation between Fe II* emission strength and Fe II equivalent width in the composite spectra assembled according to W_{FeII} . This result is striking given that the Fe II* emitter and non-emitter composite spectra in Figure 2 show pronounced differences in Fe II absorption strength. However, the fact that Fe II* emitters are preferentially at higher redshifts than Fe II* non-emitters may contribute to the stark differences in Fe II absorption strength seen in Figure 2. If the properties of interstellar gas evolve with redshift such that systems at higher redshifts show stronger resonant Fe II absorption, then one would expect that objects with strong Fe II* emission also exhibit deeper Fe II absorption profiles. We tested this hypothesis by assembling composite spectra holding A_{UV} constant and varying redshift; we find that objects at higher redshifts do exhibit preferentially stronger resonant Fe II absorption than systems at lower redshifts. This result explains the trends seen in the Fe II* emitter and non-emitter composite spectra (Figure 2) as the Fe II* emitters are both at higher redshifts and also exhibit stronger Fe II resonant absorption. In order to probe how Fe II* emission and Fe II resonant absorption relate, we must therefore look at samples at fixed redshift.

5. RESONANT MG II EMISSION

Mg II, a low ionization state of a cosmically-abundant element (Savage & Sembach 1996), is a useful tracer of interstellar gas. Mg II transitions in the rest-frame ultraviolet are commonly used as probes of galactic winds at intermediate redshifts due to their placement above the atmospheric cut-off for samples at $z \gtrsim 0.2$. In unsaturated systems, the bluer line of the Mg II doublet at $\lambda\lambda 2796, 2803 \text{ \AA}$ is twice as strong as the redder line. However, this 2:1 line ratio is not always seen in our data. Rather, we find some objects with inverted Mg II ratios (i.e., stronger absorption in the 2803 line than in the 2796 \AA line) and a majority of objects with roughly

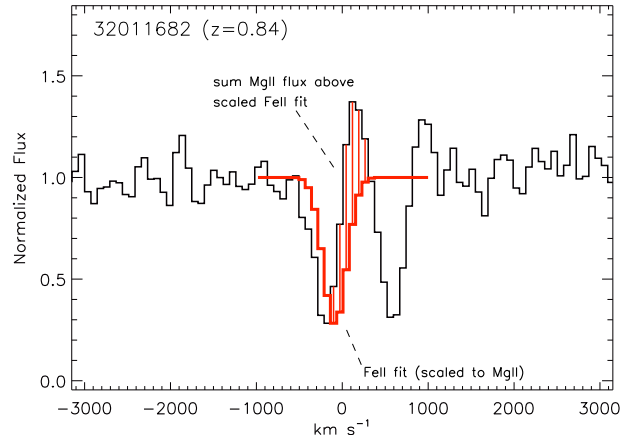


FIG. 11.— Methodology for identifying Mg II emission. We assume that the Fe II profile represents a fiducial absorption profile largely unaffected by emission filling. After normalizing the depth of the Fe II profile to that of the Mg II profile, we sum the normalized flux in the Mg II feature above the scaled Fe II profile over a range of 500 km s^{-1} , beginning at the minimum of the Fe II absorption profile. The summed flux is representative of the emission contribution of Mg II to the overall Mg II profile. This methodology is repeated for both the 2796 and 2803 \AA Mg II lines and the emission strengths of each line are added to produce a total estimate of the Mg II emission strength.

equal absorption-line strengths. The former case may be correlated with dense galactic winds, as discussed below, while the latter case indicates line saturation.

The Mg II doublet, while primarily seen in absorption, is also observed with a P-Cygni emission profile in objects as varied as Seyfert 1s (Wu et al. 1983), ultraluminous infrared galaxies (Martin & Bouché 2009), local star-forming spiral galaxies (Kinney et al. 1993), and high-redshift starburst galaxies (Weiner et al. 2009; Rubin et al. 2011; Giavalisco et al. 2011; Erb et al. 2012; Martin et al. 2012). The physical origin of Mg II emission has been attributed to several processes, including photon scattering off the backside of a galactic wind (Phillips 1993; Weiner et al. 2009; Rubin et al. 2011), where this process has also been seen in Ly α emission in Lyman break galaxies (Pettini et al. 2001; Shapley et al. 2003). Both features of the Mg II doublet can be strongly affected by emission filling due to the lack of excited ground states available for fluorescence. We examine here the diversity of Mg II profiles in our sample, focusing specifically on the incidence of Mg II emission. Even in our relatively low-resolution data, the Mg II doublet is resolved given its wide velocity separation ($\sim 770 \text{ km s}^{-1}$).

5.1. Mg II Emitters and Non-emitters

Several authors have investigated the frequency of Mg II emission in samples of star-forming galaxies. Weiner et al. (2009) report Mg II emission in 4% of their sample of $z \sim 1.4$ star-forming galaxies. Rubin et al. (2010b) find that 4/468 ($< 1\%$) star-forming galaxies at a similar epoch exhibit Mg II emission. Both of these authors identified the presence of Mg II emission in continuum-normalized spectra by comparing the fluxes above the continuum level in two wavelength windows tracing the continuum and the region immediately redward of the 2796 \AA line, respectively (Figure 3 in Weiner

et al. 2009). Weiner et al. (2009) find Mg II emission preferentially in blue, luminous galaxies and propose that the emission may be due to low-level AGNs, although these authors fail to find any emission lines characteristic of active galaxies (e.g., Ne V 3425 Å) in a co-added spectrum of all their data. Weiner et al. (2009) also assemble a composite spectrum excluding objects with individual detections of Mg II emission and still find Mg II emission in the co-added stack. These authors argue that stellar chromospheric Mg II emission is unlikely to account for the observed emission; recombination in H II regions or scattering in galactic winds are more likely causes of Mg II emission.

While the technique of Weiner et al. (2009) and Rubin et al. (2010b) robustly identifies strong Mg II emitters, it may miss objects with only weak Mg II emission. In light of the increased S/N of our data (~ 11 per resolution element) relative to that of the Weiner et al. data (~ 1 per resolution element) and the Rubin et al. data (~ 2 per resolution element), we developed a new method to systematically isolate objects with Mg II emission. Instead of relying on measurements of flux above the continuum within prescribed wavelength windows, we employed the fits to the resonant Fe II absorption features in the data (Martin et al. 2012). Since the Fe II lines we fit in our absorption-line measurements are not as susceptible to emission filling as Mg II, we used the Fe II profile for this subset of lines as a proxy for the intrinsic Mg II absorption profile free of the effects of emission filling. In Figure 11, we schematically illustrate how we compare the Mg II and Fe II profiles to estimate the contribution of Mg II emission to the overall Mg II profile. For each of the objects with a V_1 measurement and spectral coverage of Mg II, we plotted the Fe II absorption fit and the Mg II profile together in velocity space. We normalized the Fe II fit to the lowest pixel of the Mg II absorption trough and estimated the Mg II emission component by summing the positive flux between the Mg II profile and the normalized Fe II fit. We summed the flux only over a limited velocity range – from the minimum of the Fe II profile to 500 km s^{-1} redward – to ensure that the 2796 and 2803 Å lines are not artificially extended blueward or redward of the true line profile. The resulting flux measurements have units of Å, as these measurements represent areas integrating a continuum-normalized flux (unitless) with wavelength (units of Å). This method is sensitive both to strong Mg II emitters – such as those found using the technique of Weiner et al. (2009) and Rubin et al. (2010b) – and also to objects in which Mg II emission is not visually apparent but the kinematic profile of Fe II differs from that of Mg II. The ability of this technique to isolate objects with different Fe II and Mg II kinematics results in a more complete sample of Mg II emitters than was found by either Weiner et al. (2009) or Rubin et al. (2010b). Our methodology furthermore selects objects where the Mg II emission may not obviously extend above the local continuum; both Weiner et al. (2009) or Rubin et al. (2010b) used a technique in which only Mg II emission above the continuum was considered.

We searched for emission in the 2796 and 2803 Å lines separately and we assigned an emission significance to each line using the error spectrum of the data. We then

combined the emission significances of the 2796 and 2803 Å features for each object, adding their associated errors in quadrature, to obtain a total Mg II emission strength and uncertainty for each object. Of the 145 objects in our sample with a V_1 measurement and spectral coverage of both features of the Mg II doublet, 22 ($\sim 15\%$) show a combined 2796/2803 emission significance at or above the 6σ level while also exhibiting at least a 3σ emission significance in each individual line (Figure 12). We call this subsample of objects “Mg II emitters”⁸. In Martin et al. (2013), we analyze the 2D spectra and find that one of these Mg II emitters exhibits spatially-extended emission. If we instead require that Mg II emitters exhibit a 3σ detection in only at least one of the Mg II lines, we find that 57 objects ($\sim 39\%$) meet the Mg II emitter criterion. There are clearly many possible ways of isolating Mg II emitters, but the criteria we use primarily isolate objects with visually striking emission and fully utilize the information provided by our coverage of both Fe II and Mg II features.

Whereas we find that $\sim 15\%$ of objects in our sample show strong Mg II emission, Erb et al. (2012) observe that 33/96 star-forming galaxies at $1 \lesssim z \lesssim 2$ ($\sim 30\%$) exhibit strong Mg II emission. Erb et al. (2012) flagged Mg II-emitting galaxies by searching for two adjacent pixels at least 1.5σ above the continuum in either the 2796 or 2803 Å lines. This technique clearly depends on the S/N of the spectra. Our study finds a higher fraction of Mg II-emitters galaxies than both Weiner et al. (2009) and Rubin et al. (2010b) and we attribute this discrepancy to the increased sensitivity of our method to objects with different Fe II and Mg II kinematics. We assembled a spectral stack of the 22 objects in our sample exhibiting Mg II emission and find no evidence for Ne V AGN emission at 3425 Å in the 19 objects with spectral coverage of Ne V. Based on Chandra X-ray flux catalogs available for the Extended Groth Strip, only one object (out of 72 objects in this field with LRIS spectroscopy) is likely an AGN due to its X-ray flux. This object does not have spectral coverage of Mg II and therefore is not included in the above analyses.

We also isolated a sample of 34 “Mg II non-emitters” with $< 2\sigma$ Mg II emission detections, where we required that each object have a continuum S/N greater than the lowest S/N observed in the Mg II emitter sample (4.66 pixel^{-1}). This methodology of requiring comparable continuum S/N in the Mg II emitter and non-emitter samples ensures that objects do not scatter into the Mg II non-emitter sample purely because of noise. Three Mg II non-emitters have colors indicative of “green valley” galaxies; our conclusions remain unchanged if these objects are removed from the non-emitter sample. In

⁸ While 18/22 Mg II emitters show stronger emission in the 2796 Å line than in the 2803 Å line – consistent with expectations based on oscillator strengths – four objects show more emission in the 2803 Å line. These line ratios, which deviate from what is expected based on oscillator strengths ($f_{12} = 0.608$ for the 2796 Å line and $f_{12} = 0.303$ for the 2803 Å line), are predicted to occur more frequently in cases where a higher density of particles populates the galactic wind (Prochaska et al. 2011). Higher quality data are necessary in order to determine if a population of objects with inverted emission ratios exists, as suggested by Prochaska et al. (2011), or if our finding is simply the result of the limited S/N of our data set.

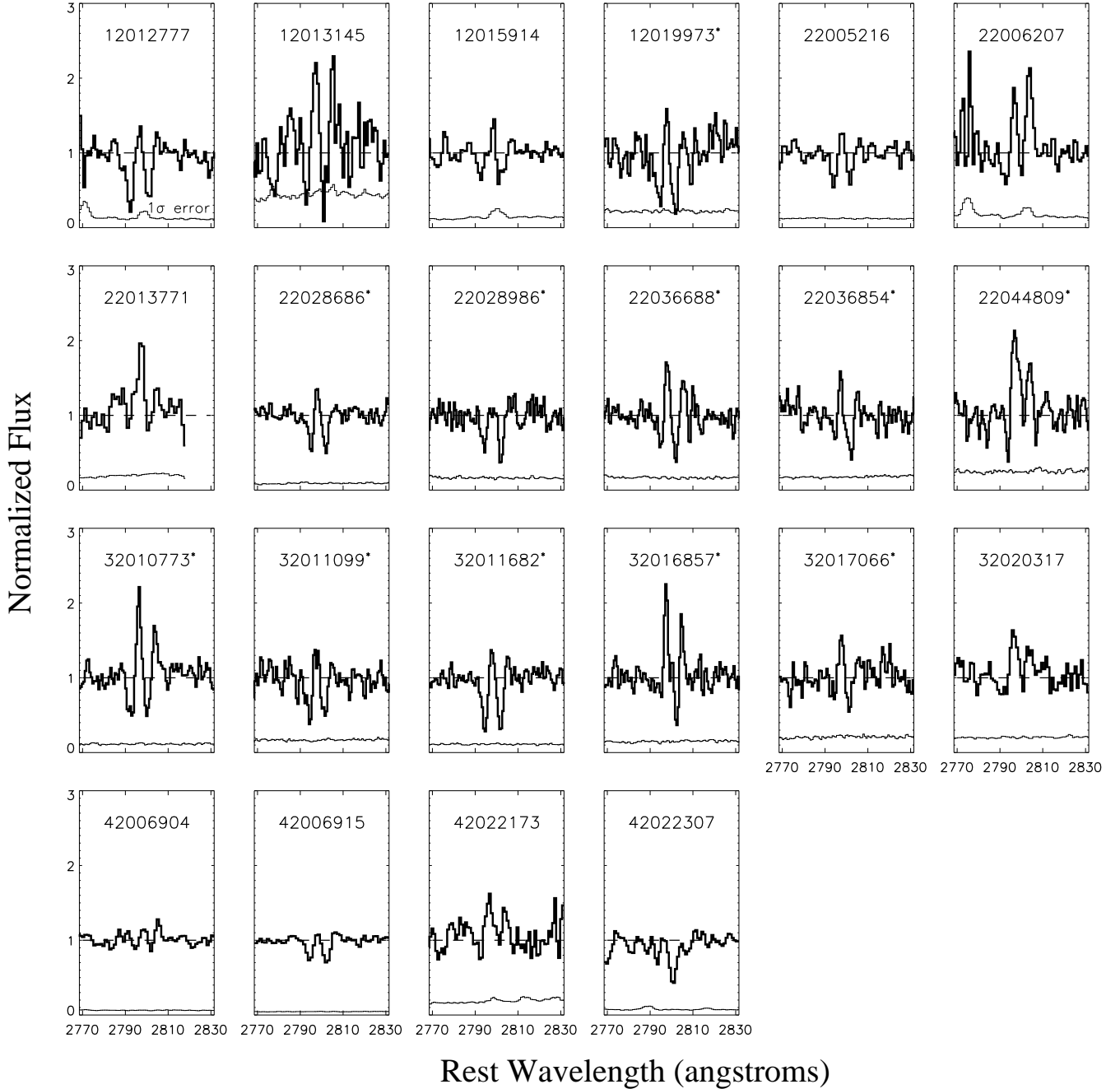


FIG. 12.— Thumbnails of the 22 objects with significant Mg II emission, selected using the method described in Section 5.1. The majority of objects show pronounced Mg II emission above the continuum, where the continuum is indicated by the dashed horizontal line. Object ID numbers followed by an asterisk indicate that the object was observed with the d560 dichroic and the 600 line mm^{-1} grating while object numbers lacking an asterisk correspond to galaxies observed with the d680 dichroic and the 400 line mm^{-1} grating and the 800 line mm^{-1} grating. These spectra are unsmoothed. The 1σ error spectra are shown below the data spectra; the average S/N of the Mg II emitters is 7.5 (12.0) pixel^{-1} for the d560 (d680) samples.

Figure 13, we plot composite spectra assembled from Mg II emitters and non-emitters, respectively. While Fe II* emission is stronger in the stack of Mg II emitters, the composite spectra are otherwise comparable in terms of Fe II kinematics and strength.

According to radiative transfer modeling by Prochaska et al. (2011), the geometry of galactic winds affects the strength of Mg II emission. Specifically, the opening angle of the wind, assuming a biconical outflow geometry, modulates the strength of Mg II

emission. More collimated outflows show weaker Mg II emission while more isotropic outflows show stronger Mg II emission. The 22 objects in our sample that show significant Mg II emission are therefore expected to have gas flows opening into large solid angles. As objects with wide-angle gas flows should show kinematic signatures of galactic winds more frequently than systems with more collimated flows, we checked the frequency of 1σ and 3σ detections of gas flows in the sample of Mg II emitters. We find that 59% (50%) of Mg II emitters show 1σ (3σ)

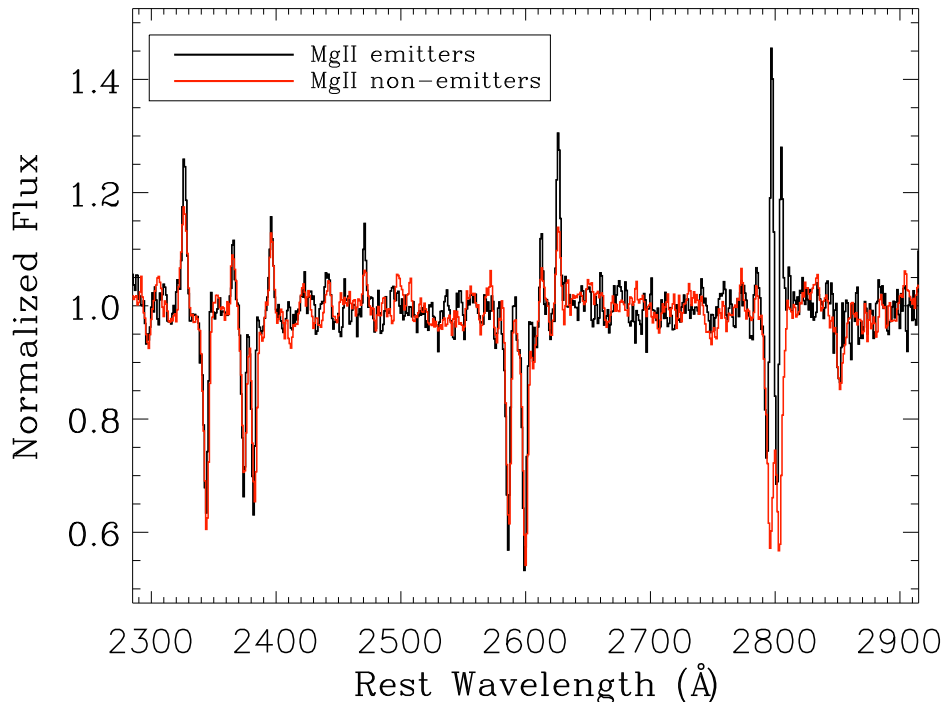


FIG. 13.— Comparison of composite spectra assembled from stacks of the 22 Mg II emitters (black) and 34 Mg II non-emitters (red). On average, Mg II emitters show stronger Fe II* emission than objects with weaker Mg II emission. Typical errors on the Mg II emitter (non-emitter) composite spectra are 0.03 (0.02) in units of normalized flux.

gas flows, compared with 67% (27%) of the sample as a whole. These results show that the frequency of objects exhibiting strong ($\geq 3\sigma$) gas flows is higher in the Mg II emitter sample than in the parent sample. Therefore, our data do support the hypothesis of Prochaska et al. (2011) that more isotropic outflows are associated with stronger Mg II emission. Observations with upcoming integral field units on large telescopes (e.g., the Keck Cosmic Web Imager (KCWI; Martin et al. 2010) and the Multi Unit Spectroscopic Explorer (MUSE; Bacon et al. 2010) on the VLT) will be important for determining the geometry of Mg II emission.

We measured the kinematics of the Mg II emission peaks in the composite spectrum assembled from the 22 objects showing significant Mg II emission. We fit a Gaussian profile to the 2796 and 2803 Å features separately and find that the emission peaks are located at 111 ± 16 and 168 ± 30 km s $^{-1}$, respectively. Weiner et al. (2009) and Rubin et al. (2010b) also note Mg II emission peaks redshifted by approximately ~ 100 km s $^{-1}$ in their composite spectra of star-forming galaxies at $z \sim 1.4$ and $0.7 < z < 1.5$, respectively.

5.2. Mg II Emission Strength and Galaxy Properties

As strong Mg II emission is only seen in a subset of our sample, we investigate here the galaxy properties modulating Mg II emission. In the left-hand panel of Figure 14, we show a color-magnitude diagram with the 22 Mg II emitters and the 34 Mg II non-emitters highlighted. We find that the galaxies showing strong Mg II emission are preferentially bluer ($\langle U - B \rangle = 0.44 \pm 0.02$) and lower stellar mass ($\langle M_* \rangle = 1.0 \pm 0.2 \times 10^{10} M_\odot$) than both

Mg II non-emitters ($\langle U - B \rangle = 0.67 \pm 0.03$, $\langle M_* \rangle = 4.1 \pm 0.9 \times 10^{10} M_\odot$) and the global sample of objects with comparable S/N in their LRIS spectra ($\langle U - B \rangle = 0.60 \pm 0.02$, $\langle M_* \rangle = 3.3 \pm 0.4 \times 10^{10} M_\odot$); the errors on these colors represent the standard deviation of the mean. Martin et al. (2013) discuss one Mg II emitter with spatially-extended Mg II emission and remark that this object has a notably blue $U - B$ color and a stellar mass falling in the lowest third of the sample.

Weiner et al. (2009) find that objects at $z \sim 1.4$ showing Mg II in emission are typically drawn from a bluer and more luminous population. To test if our own data also show Mg II emitters being more luminous than the sample as a whole, we conducted a KS test comparing the distributions of the B -band absolute luminosities of the 22 objects with significant Mg II emission and the entire sample of objects with V_1 measurements and spectral coverage of Mg II. We find a probability of $\sim 30\%$ that the two distributions are drawn from the same parent population. Our data accordingly do not suggest an intrinsic luminosity difference between objects showing Mg II in emission and the general population, although we acknowledge that our sample is substantially smaller than that of Weiner et al. (2009).

As a corollary to the analyses in Section 4.3 investigating the links between Fe II* emission and galaxy properties, we now turn to systematically analyzing how a variety of galaxy properties are correlated with Mg II emission strength. We showed above that individual objects with strong Mg II emission have bluer colors and lower stellar masses than the sample as a whole (Figure 14), consistent with the results of Martin et al. (2012) based

on both composite and individual spectra. Now, we employ composite spectra to investigate how the strength of Mg II emission varies as a function of different galaxy properties. We included 17 of the galaxy properties used for the Fe II* analysis in Section 4.3, where we omitted the Mg II emission strength property. Instead of Mg II emission strength, we used Fe II* emission strength. In the 18 pairs of composite spectra assembled according to these galaxy properties, we measured the strength of Mg II emission using the same technique employed for measuring Mg II emission in the individual spectra (Section 5.1). We then calculated the change in Mg II emission strength between each pair of composite spectra using a method analogous to that employed for Fe II* in Section 4.3. The quantity D_{MgII} is defined as the difference in Mg II emission flux between each pair of composite spectra:

$$D_{\text{MgII}} = \Delta(f_{2796} + f_{2803}) \quad (2)$$

where f_{2796} and f_{2803} are the emission fluxes in each Mg II line. In Figure 15, we show the values of D_{MgII} for the 18 galaxy parameters. We observe D_{MgII} ranging from 0.1–1.0 Å. The uncertainty on D_{MgII} , δD_{MgII} , was calculated from the individual errors on the Mg II flux measurements. Propagating errors through Equation 2, we find that δD_{MgII} ranges from 0.09–0.19 Å, with a sample average of 0.15 Å.

Nine galaxy properties modulate Mg II emission at or above the 3σ level: sSFR, $\sigma_{[\text{OII}]}$, $W_{[\text{OII}]}$, 1σ gas flows, Fe II* emission strength, W_{FeII} , A_{UV} , M_* , and disk inclination i . Stronger Mg II emission is observed in objects with higher sSFR, lower $\sigma_{[\text{OII}]}$, larger $W_{[\text{OII}]}$, 1σ outflows (as opposed to 1σ inflows), stronger Fe II* emission, smaller W_{FeII} , lower A_{UV} , lower M_* , and lower inclination.

Five of the above properties – sSFR, $\sigma_{[\text{OII}]}$, $W_{[\text{OII}]}$, A_{UV} , and M_* – describe the stellar and H II region properties of galaxies and we focus on these five properties for the following analyses. In Figure 16, we show composite spectra assembled according to these five properties. In each case, stronger Mg II emission is accompanied by stronger Fe II* emission (unsurprising since stronger Fe II* emission is found to be statistically correlated with stronger Mg II emission). We show in Figure 17 individual measurements of Mg II emission versus measurements of sSFR, $\sigma_{[\text{OII}]}$, $W_{[\text{OII}]}$, A_{UV} , and M_* , respectively. The correlation significances and Spearman rank-order correlation coefficients are as follows: $[3.0\sigma, 0.50]$, $[3.6\sigma, -0.30]$, $[4.4\sigma, 0.38]$, $[1.2\sigma, -0.21]$, and $[3.5\sigma, -0.30]$. The strongest correlation (4.4σ) is observed between Mg II emission strength and $W_{[\text{OII}]}$. As the sample sizes of objects with sSFR and A_{UV} information are roughly one fourth those of the samples with $\sigma_{[\text{OII}]}$, $W_{[\text{OII}]}$, or M_* measurements, is important to remember that the correlation significances of Mg II emission with either sSFR or A_{UV} will necessarily be lower simply due to smaller number statistics. We re-calculated the correlation significances of Mg II emission strength and $\sigma_{[\text{OII}]}$, $W_{[\text{OII}]}$, and M_* , respectively, including only objects also having sSFR and A_{UV} measurements. The correlation significances and Spearman rank-order correlation coefficients are as follows: $[2.0\sigma, -0.34]$, $[2.3\sigma, 0.42]$, and $[1.9\sigma, -$

$0.32]$. We find that the strongest correlation, when equal sample sizes are compared, is between Mg II emission strength and sSFR (3.0σ). In Figure 18, we show histograms of sSFR, $\sigma_{[\text{OII}]}$, $W_{[\text{OII}]}$, A_{UV} , and M_* , highlighting Mg II emitters and non-emitters. A clear distinction between Mg II emitters and non-emitters is observed in $\sigma_{[\text{OII}]}$, $W_{[\text{OII}]}$, and M_* parameter space, but the smaller sample size of objects with sSFR and A_{UV} information makes it difficult to definitively discern a difference in the sSFR and A_{UV} properties of Mg II emitters and non-emitters. In Figure 19, we show the intercorrelations of sSFR, $\sigma_{[\text{OII}]}$, $W_{[\text{OII}]}$, A_{UV} , and M_* . As in the case of SFR, A_{UV} , and $W_{[\text{OII}]}$ modulating Fe II* emission strength, all the significant correlations are in consistent senses. In other words, there is overlap between objects with high sSFR, low $\sigma_{[\text{OII}]}$, high $W_{[\text{OII}]}$, low A_{UV} , and low M_* such that a single property could be modulating these intercorrelations and the trends of sSFR, $\sigma_{[\text{OII}]}$, $W_{[\text{OII}]}$, A_{UV} , and M_* with Mg II emission strength. In the next section, we show that sSFR appears to drive variations in Mg II emission. We note that the correlation observed between sSFR and Mg II emission cannot arise simply as a result of the methods used for estimating these two quantities. As sSFR is defined as the dust-corrected SFR normalized by stellar mass, it turns out to be weakly correlated with the observed UV-continuum luminosity density. Mg II emission strength is based on the Mg II emission-line flux divided by the UV-continuum luminosity density. Accordingly, for fixed Mg II emission-line flux, one expects lower Mg II emission strengths for objects with higher sSFR (contrary to what we observe).

While we have focused here on the relationships between the stellar and H II region properties of galaxies and the strength of Mg II emission, it is also important to understand how the strength of interstellar absorption – in this case, parameterized by W_{FeII} – is correlated with the strength of interstellar emission. Other authors have studied how the strengths of resonant emission and absorption lines are linked; we continue this investigation here motivated by the fact that our data include several strong resonant lines of both Fe II and Mg II. In a sample of Lyman break galaxies at $z \sim 3$, Shapley et al. (2003) noted that objects showing weaker Ly α emission had larger interstellar Si II, C II, Fe II, and Al II absorption equivalent widths while objects marked by stronger Ly α emission had correspondingly weaker interstellar absorption lines. These authors attributed these trends to different covering fractions of dusty clouds, where galaxies with higher cloud covering fractions typically suffer more extinction (reducing the Ly α emission strength and increasing the interstellar absorption equivalent width). In a lower-redshift sample ($\langle z \rangle = 2.3$), Erb et al. (2006) found that higher-mass galaxies showed stronger interstellar absorption lines and weaker Ly α emission, consistent with the results from Shapley et al. (2003). Martin et al. (2012) furthermore observed that higher-mass galaxies exhibit characteristically stronger Mg II absorption lines. We also find here – in the same data set used by Martin et al. (2012) – that objects with stronger Mg II emission show weaker Fe II absorption (Figure 13). Additionally, we recover a statistically significant D_{MgII} value (0.40 ± 0.11 Å) when we divide objects on the basis of W_{FeII} and measure their

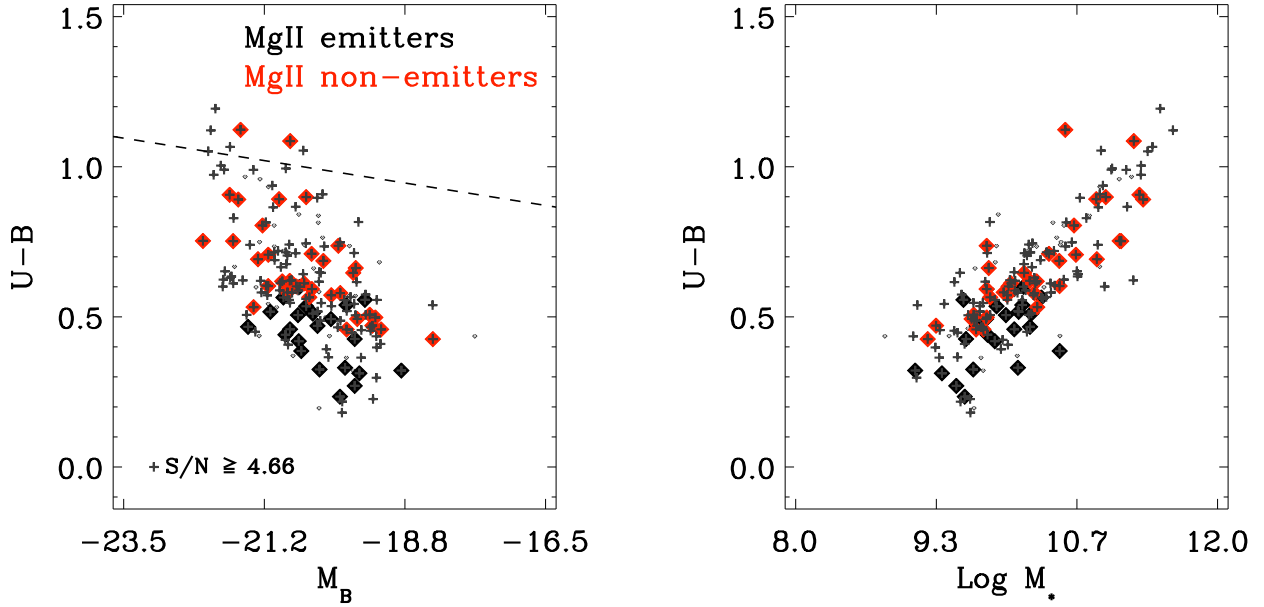


FIG. 14.— Left: color-magnitude diagram with the 22 Mg II emitters shown as filled black diamonds and the 34 Mg II non-emitters shown as filled red diamonds. Gray crosses indicate objects with $S/N > 4.66$ pixel $^{-1}$, the minimum S/N of the Mg II emitter sample. Consistent with the results of Weiner et al. (2009) and Martin et al. (2012), we find that objects showing Mg II in emission are bluer than the general galaxy population: the Mg II emitters have an average $U - B$ color of 0.44 ± 0.02 compared with an average $U - B$ color of 0.67 ± 0.03 for the Mg II non-emitters. The global sample of objects is characterized by an average $U - B$ color of 0.60 ± 0.02 , where these errors represent the standard deviation of the mean. Right: color versus stellar mass plot, where the symbols are the same as in the left panel. Mg II emitters have characteristically lower stellar masses ($\langle M_* \rangle = 1.0 \pm 0.2 \times 10^{10} M_\odot$) than both objects with weaker Mg II emission ($\langle M_* \rangle = 4.1 \pm 0.9 \times 10^{10} M_\odot$) and the population as a whole ($\langle M_* \rangle = 3.3 \pm 0.4 \times 10^{10} M_\odot$), consistent with the results of Martin et al. (2012).

Mg II emission strengths; objects with larger Fe II absorption equivalent widths have weaker Mg II emission. These findings support the results of both Shapley et al. (2003) and Erb et al. (2006) and suggest that Mg II emission is stronger when the covering fraction of interstellar gas is lower.

6. DISCUSSION

We have shown that fine-structure Fe II* and resonant Mg II emission are characteristic of star-forming galaxies at $z \sim 1$. In this section, we build on our previous analyses of the correlations of Fe II* and Mg II emission strength with galaxy properties. We propose physical explanations for these observed correlations and suggest that galaxies with strong Fe II* or Mg II emission have typically lower A_{UV} , higher sSFR, and lower M_* than the galaxy population as a whole. We conclude this section with a discussion of the striking absence of Fe II* emission in local galaxies and argue that slit losses may be largely responsible for the lack of Fe II* emission in nearby objects.

6.1. Fe II* Emission is Modulated by Dust

Several authors have proposed explanations for the variety of Fe II* emission strengths observed in star-forming galaxies, including slit losses (Giavalisco et al. 2011; Erb et al. 2012), viewing angle effects of observing a non-spherical wind (e.g., Erb et al. 2012), and dust attenuation (Prochaska et al. 2011). We address each of these explanations in turn and examine how our results – that systems at higher redshifts and those with lower SFRs, lower A_{UV} values, and larger $W_{[OII]}$ measurements

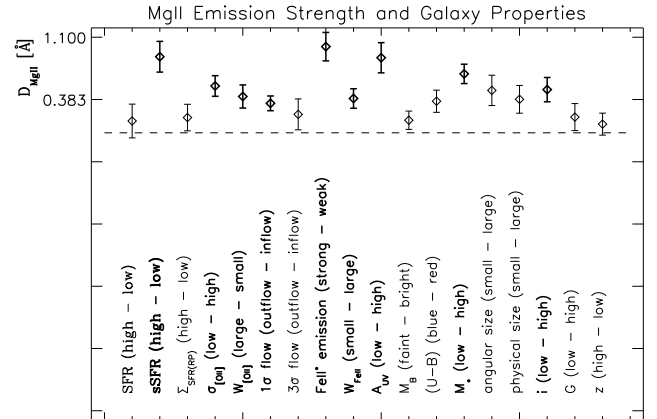


FIG. 15.— Variation of Mg II emission strength with galaxy properties. D_{MgII} , a parameterization of the change in Mg II emission strength between two spectra, is shown for pairs of composite spectra assembled according to 18 different galaxy properties. The largest D_{MgII} values, significant at $> 3\sigma$, are observed for nine intrinsic properties: sSFR, $\sigma_{[OII]}$, $W_{[OII]}$, 1σ gas flows, Fe II* emission strength, W_{FeII} , A_{UV} , M_* , and disk inclination i (bold text). Stronger Mg II emission is observed in objects with higher sSFR, lower $\sigma_{[OII]}$, larger $W_{[OII]}$, 1σ outflows, stronger Fe II* emission, smaller W_{FeII} , lower A_{UV} , lower M_* , and lower i .

show stronger Fe II* emission – support or do not support these hypotheses.

As discussed later in this section, the striking absence of Fe II* emission in local galaxies has been attributed to slit losses (Giavalisco et al. 2011; Erb et al. 2012).

Erb et al. (2012) measured the spatial extent of Fe II* emission in a sample of star-forming galaxies at $1 \lesssim z \lesssim 2$ and found that Fe II* emission may be more spatially extended than the continuum, consistent with the hypothesis that Fe II* emission may be missed by narrow spectroscopic slits. In Figure 20, we show that dividing objects on the basis of angular size (i.e., simulating the effects of slit losses) yields a difference in Fe II* strength at the 1.8σ level such that smaller objects show stronger Fe II* emission. However, the trend of Fe II* emission strength with angular size is less significant than the trends of Fe II* emission strength with SFR, A_{UV} , $W_{[OII]}$, and z . We accordingly conclude that slit losses may be partially responsible for the variety of Fe II* emission strengths observed in our sample, but that other galaxy properties play a larger role in the regulation of Fe II* emission. It is important to emphasize that the effects of slit losses will be more pronounced over a larger redshift baseline (i.e., between local samples and $z \sim 1$) than is spanned by our current data set.

Fe II* emission can also be modulated by viewing angle effects of observing a non-spherical galactic wind. A biconical outflow will show variations in emission strength depending on the viewing geometry of the observer with respect to the wind (Erb et al. 2012). For a wind arising perpendicular to a galaxy disk, these authors propose that observations of the wind face-on will yield stronger absorption signatures and weaker emission measurements while the wind viewed edge-on will predominantly show emission. The model predictions make sense given that a wind seen face-on means that the observer is looking down the barrel and therefore seeing material absorbed against the background light of the host galaxy. Conversely, observations of a wind edge-on see the wind projected 90° to the line of sight and accordingly observe more scattered emission as opposed to absorption backlit by starlight.

In our sample, we find that objects showing stronger Fe II* emission also show more blueshifted Mg II absorption (Figure 2). This result is contrary to the model presented by Erb et al. (2012), in which stronger emission lines would be more prevalently seen in edge-on systems not expected to show large blueshifts in their interstellar absorption lines. As Martin et al. (2012) estimated that the geometry of galactic winds at $z \sim 1$ is roughly biconical with a wind opening angle of $\sim 40^\circ$, disk inclination and the observability of interstellar blueshifts should be correlated. Disk inclination estimates are available for 46 objects in our sample and we assemble composite spectra from samples of both high- and low-inclination objects, where we divide the sample at $i = 45^\circ$. The average inclination of the two samples are $\langle i \rangle = 58^\circ$ and 38° , respectively. We find no significant change in Fe II* emission strength in the samples divided on the basis of disk inclination, although our sample is small. While we do not find a trend between disk inclination and Fe II* emission strength, we do find a trend at the $\sim 3.6\sigma$ level between disk inclination and Mg II emission strength such that systems with low disk inclinations (i.e., more face on) show stronger Mg II emission. The $\sim 10^\circ$ uncertainties on our inclinations – where inclination was estimated from rest-frame ultraviolet imaging sensitive only to current episodes of star formation – make it difficult to construct subsamples that are precisely divided according to

viewing angle.

The absorption of photons by dust additionally modulates Fe II* emission. Prochaska et al. (2011) modeled Fe II* emission lines arising from galactic winds and found that increasing dust attenuation suppressed Fe II* emission (although resonant Fe II absorption was minimally affected by changes in attenuation). These authors proposed that emission-line fluxes are reduced by a factor of order $(1 + \tau_{\text{dust}})$, where $\tau_{\text{dust}} = A_V/1.086 \sim A_{UV}/1.9$ assuming a Calzetti et al. (2000) dust attenuation law. The 54 objects in our sample with dust attenuation measurements have A_{UV} values ranging from 0.02–4.55, with a median A_{UV} of 1.8 and a corresponding median τ_{dust} of ~ 0.9 . When we divide our data on the basis of A_{UV} , we find that objects with stronger dust attenuation show $\sim 40\%$ weaker Fe II* emission (Figure 5), in rough agreement with predictions by Prochaska et al. (2011). The other three galaxy properties that are significantly correlated with Fe II* emission strength – SFR, $W_{[OII]}$, and z – are themselves correlated with A_{UV} (Figure 10). As galaxies at larger redshifts with lower SFRs and larger $W_{[OII]}$ measurements have lower A_{UV} values, our results are consistent with a single parameter – A_{UV} – being the primary driver of Fe II* emission strength.

In order to further investigate if A_{UV} is most strongly driving the variation in Fe II* emission, we assembled composite spectra holding A_{UV} constant and varying SFR, $W_{[OII]}$, and z respectively. If A_{UV} is indeed primarily responsible for modulating Fe II* emission, then we expect these spectra to show weaker changes in Fe II* emission compared with composite spectra holding SFR, $W_{[OII]}$, and z constant, respectively, and varying A_{UV} . We do find that the spectra holding A_{UV} constant show weaker changes in Fe II* emission strength ($D_{\text{FeII}^*} = 0.12\text{--}0.28 \text{ \AA}$) than the spectra holding SFR, $W_{[OII]}$, or z constant and varying A_{UV} ($D_{\text{FeII}^*} = 0.42\text{--}0.72 \text{ \AA}$). These results are consistent with A_{UV} being the primary driver of Fe II* emission variation.

As Fe II* emission is thought to both originate in galaxy halos and also be strongly modulated by dust attenuation, it is important to understand the spatial distribution of dust in galaxy halos. In Section 4.2, we showed that our kinematic measurements of Fe II* are consistent with Fe II* emission arising in either stationary H II regions or extended galactic winds (Prochaska et al. 2011). Given the spatial extent of Fe II* emission reported by Erb et al. (2012), we choose to focus on the physical picture of emission presented by Rubin et al. (2011) in which Fe II* emission is created by photon scattering at spatial distances of $\sim \text{kpc}$ from the galactic disk. Assuming that Fe II* emission arises at large galactocentric distances, it is surprising that we find a strong correlation between Fe II* emission strength and A_{UV} . Our measurements of dust attenuation are based on observations of star-forming regions and these values are accordingly indicative of attenuation only near galactic disks.

Several authors have reported that dust is present at significant distances from galaxy disks. Nelson et al. (1998) stacked *Infrared Astronomical Satellite* profiles of local galaxies and found that $100\mu\text{m}$ emission tracing dust extended $\sim 20\text{--}30 \text{ kpc}$. Holwerda et al. (2009) studied a pair of occulting galaxies in which light from the background galaxy at $z = 0.06$ was used to probe

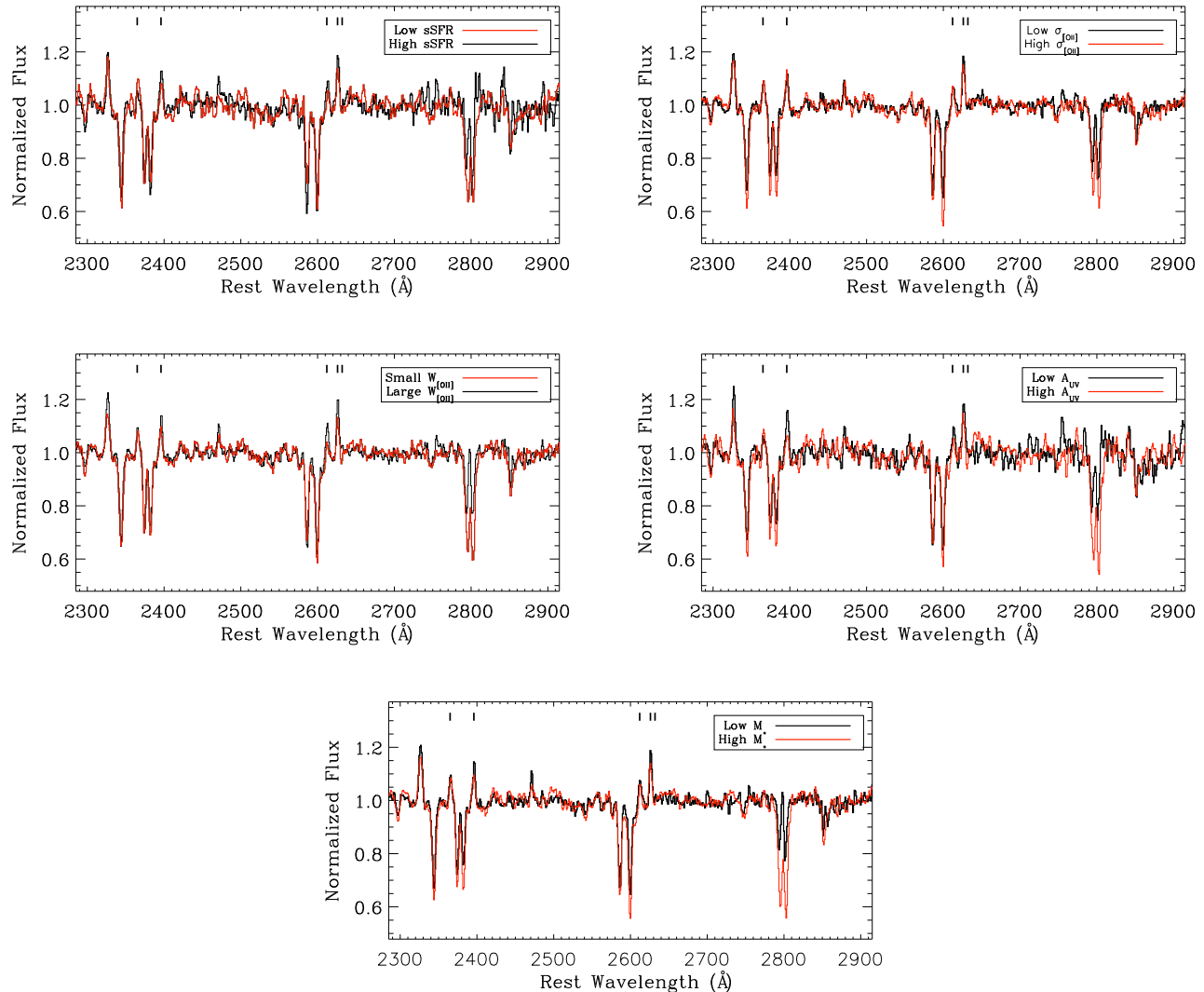


FIG. 16.— Composite spectra of key galaxy parameters that strongly modulate Mg II emission strength. Spectra are shown assembled according to sSFR, $\sigma_{[\text{OII}]}$, $W_{[\text{OII}]}$, A_{UV} , and M_* . In each case, the composite spectrum with stronger Mg II emission is plotted in black.

the extended halo of the foreground object. These authors found dust extinction in the foreground galaxy at $\sim 6R_{50}$, where R_{50} is the galaxy’s effective radius. In a large sample of background quasars and foreground galaxies, Ménard et al. (2010) inferred the presence of dust on scales from 20 kpc to a few Mpc around galaxies. These authors find that the dust mass in galaxy halos is comparable to the dust mass in galaxy disks. Dust is clearly present at significant distances from galaxies. As the A_{UV} values estimated for our sample are based on observations of star-forming regions, it is remarkable that we observe a strong correlation between A_{UV} and Fe II* emission strength. There is no *a priori* reason that the dust attenuation around star-forming regions has to be representative of the dust attenuation in the extended halo, although winds removing gas from galaxies may well entrain dust as well (e.g., Heckman et al. 2000). Future observations of spatially-resolved emission around galaxies will be instrumental for estimating the dust attenuation at large galactocentric distances.

We have shown that attenuation by dust is a leading candidate to explain the diversity of Fe II* emission strengths in star-forming galaxies at $z \sim 1$. However, it is important to acknowledge that our estimates of both galaxy angular size and disk inclination (i.e., quantities used to test the alternate hypotheses of slit losses and viewing angle effects, respectively) may be uncertain given the rest-frame ultraviolet data from which these values were calculated. As ultraviolet emission traces only high-mass star formation, galaxies typically appear more clumpy in ultraviolet passbands although this effect is strongest at $z \gtrsim 2$ (e.g., Law et al. 2007). Future analyses of angular size and disk inclination using longer wavelength data, paired with a larger sample size of objects with A_{UV} measurements, will be nonetheless important in verifying the role of dust and other properties in modulating Fe II* emission at $z \sim 1$.

6.2. Galaxy Properties Correlated with Mg II Emission Strength

TABLE 2
SUMMARY OF COMPOSITE SPECTRA

Name	Number of Objects	Fraction of Global Sample	Figure
Global sample	212	100%	1, 22
Fe II* emitters	13	6%	2
Fe II* non-emitters	9	4%	2
Mg II emitters	22	10%	12, 13
Mg II non-emitters	34	16%	13
SFR [†]	54	25%	8
sSFR [†]	54	25%	16
$\Sigma_{\text{SFR}}(\text{R}_P)$ [†]	40	19%	...
$\sigma_{[\text{OII}]}$ [†]	206	97%	16
$W_{[\text{OII}]}$ [†]	189	89%	8, 16
Inflows at 1σ	33	16%	...
Outflows at 1σ	84	40%	...
Inflows at 3σ	11	5%	...
Outflows at 3σ	35	17%	...
Mg II emission [†]	165	78%	...
W_{FeII} [†]	203	96%	...
A_{UV} [†]	54	25%	5, 8, 16
M_B [†]	212	100%	...
$U - B$ [†]	212	100%	...
M_* [†]	212	100%	16
Angular size [†]	51	24%	20
Physical size [†]	51	24%	...
Inclination [†]	54	25%	...
G [†]	53	25%	...
z [†]	212	100%	8

[†] The sample for this parameter was divided in half at the median value in order to produce the composite spectra.

The spectra in our sample exhibit a range of Mg II profiles, with some objects showing only absorption and others presenting strong emission peaks in both the 2796 and 2803 Å lines. Approximately 15% of objects show robust Mg II emission, defined as a combined 2796/2803 Å emission significance of at least 6σ above the scaled Fe II absorption profile (Section 5.2). From the color-magnitude and color-mass diagrams in Figure 14, we conclude that Mg II emission is prevalent in bluer systems with lower M_* , consistent with the results of Weiner et al. (2009), Erb et al. (2012), and Martin et al. (2012). We do not find, however, that objects separate in luminosity space based on the presence or absence of Mg II emission, as Weiner et al. (2009) do. We acknowledge that our sample is substantially smaller than the Weiner et al. (2009) data set and that we furthermore select objects showing Mg II emission not above the continuum – like Weiner et al. (2009) do – but rather above the scaled Fe II absorption profile.

We also examined the strength of Mg II emission in a suite of composite spectra assembled according to 18 different galaxy properties. We find that Mg II emission is stronger in objects characterized with lower A_{UV} , lower M_* , higher sSFR, lower $\sigma_{[\text{OII}]}$, and larger $W_{[\text{OII}]}$. Mg II emission is also stronger in galaxies with 1σ outflows (as opposed to inflows), stronger Fe II* emission, smaller W_{FeII} , and smaller disk inclinations, although these four properties are not direct tracers of the stellar or H II region properties of galaxies (Section 5.2). Considering the ensemble of five galaxy properties reflective of stellar environments, we assembled a variety of composite spectra in order to determine if one property in particular was re-

sponsible for most of the variation in Mg II emission. We constructed 40 spectra in total, five groups of eight composite spectra each. The groups consisted of composite spectra holding one property constant and modulating the remaining four properties (4 properties \times a binary division of each = 8 composite spectra). In each of these 40 composite spectra, we systematically measured the strength of Mg II emission and then calculated D_{MgII} for each pair of spectra (Section 5.2). We find that when A_{UV} , M_* , $\sigma_{[\text{OII}]}$, and $W_{[\text{OII}]}$ are held constant, the largest D_{MgII} values are observed for the pairs of spectra divided by sSFR. In other words, sSFR appears to more strongly modulate Mg II emission than A_{UV} , M_* , $\sigma_{[\text{OII}]}$, or $W_{[\text{OII}]}$. Additional evidence that sSFR may drive the variation in Mg II emission strength comes from the correlation significances between Mg II emission and sSFR, $\sigma_{[\text{OII}]}$, $W_{[\text{OII}]}$, A_{UV} , and M_* shown in Figure 17. When the sSFR, $\sigma_{[\text{OII}]}$, $W_{[\text{OII}]}$, A_{UV} , and M_* samples are normalized to a common size, we find the strongest correlation between Mg II and sSFR (3.0σ).

For completeness, we also investigated other galaxy properties besides sSFR that may be additionally modulating Mg II emission strength. Based on the measurements of the composite spectra presented in Figure 15, we find that the galaxy properties showing the strongest absolute variation in Mg II emission strength are M_* and Fe II* emission strength. Each of these two properties are correlated with Mg II emission at $> 6\sigma$, while the remaining seven properties, including sSFR, are correlated with Mg II emission at $\lesssim 5\sigma$. Given that Fe II* emission is likely modulated by A_{UV} (Section 6.1), we investigate here how M_* and A_{UV} are correlated with Mg II emission strength. In Figure 21, we show composite spectra

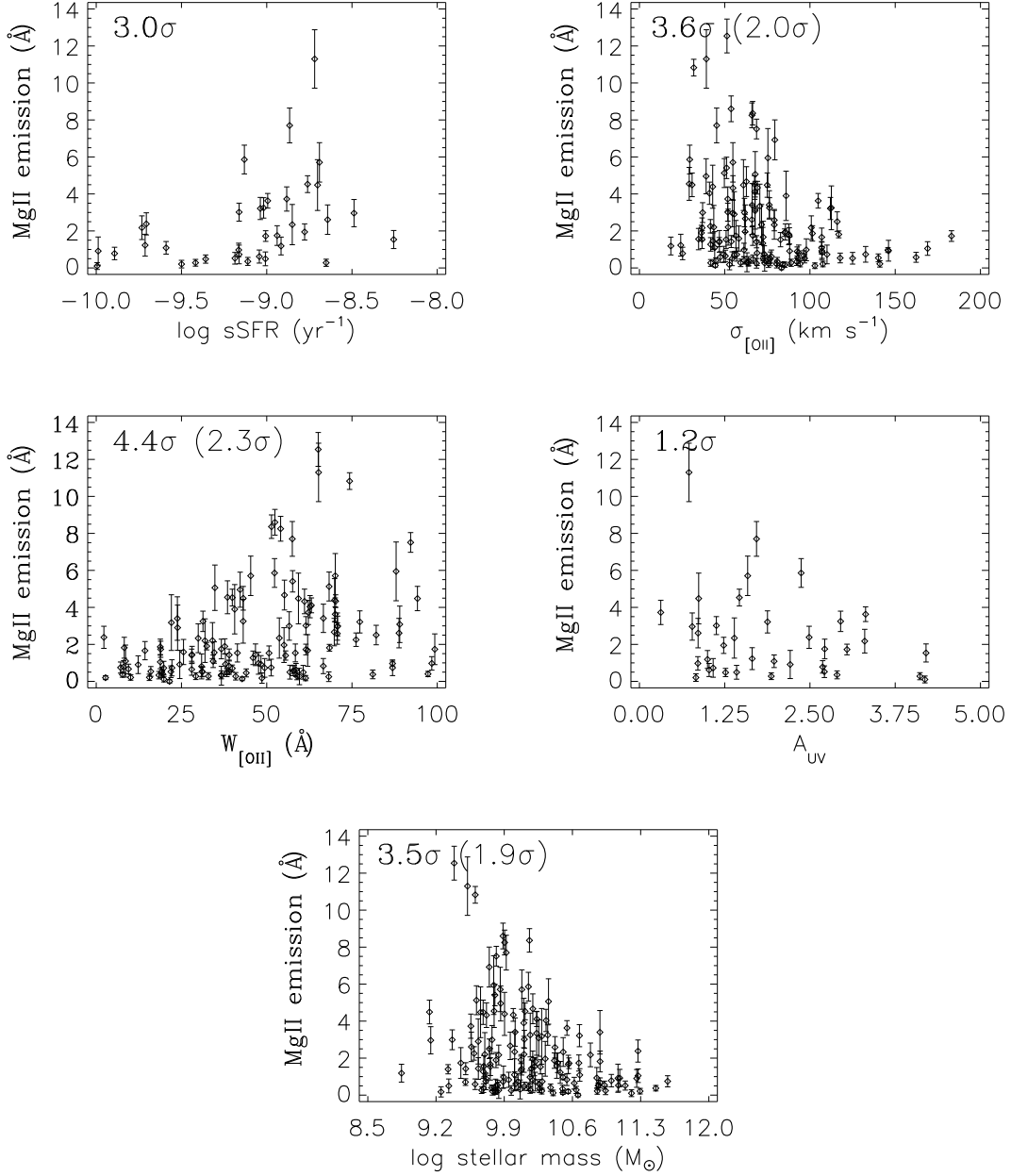


FIG. 17.— Mg II emission strength versus sSFR, $\sigma_{[\text{OII}]}$, $W_{[\text{OII}]}$, A_{UV} , and M_* , respectively. Strong correlations ($\geq 3\sigma$) are found between Mg II emission strength and sSFR, $\sigma_{[\text{OII}]}$, $W_{[\text{OII}]}$, and M_* , such that objects with pronounced Mg II emission tend to have larger sSFR, lower $\sigma_{[\text{OII}]}$, larger $W_{[\text{OII}]}$, and lower M_* . As fewer objects have sSFR and A_{UV} measurements, we also calculated correlation significances inclusive only of objects with these measurements. The results of these analyses are shown in parentheses; the strongest correlation, adjusted for sample size, is between Mg II emission strength and sSFR. Four objects with high sSFRs and low A_{UV} values appear to drive the correlations between Mg II emission and sSFR and A_{UV} , respectively; these objects are otherwise unremarkable in both their spectra and images.

assembled holding M_* (A_{UV}) constant and varying A_{UV} (M_*). If one galaxy property was responsible for controlling the bulk of Mg II emission variation, we would expect to find only minimal changes in Mg II emission strength when that property is held constant. Rather, we find that Mg II emission strength changes when M_* is held constant and also when A_{UV} is held constant. These results suggest that both M_* and A_{UV} modulate Mg II emission strength and that neither parameter dom-

inates in controlling Mg II emission. Even so, the composite spectra divided by A_{UV} show more consistent variation in their Mg II profiles than the composite spectra divided by M_* , suggestive that A_{UV} modulates Mg II more strongly than M_* . Prochaska et al. (2011) develop models of galactic winds in which the presence of dust affects the incidence of Mg II emission, where dustier systems show significantly less emission. These authors note that the Mg II doublet is particularly susceptible

to attenuation by dust since resonant photons scatter and experience longer path lengths – and therefore more opportunities for encountering a dust grain – than non-resonant photons, akin to the case of Ly α (Kornei et al. 2010).

We conclude that a typical Mg II emitter has some characteristic properties: it has a higher sSFR, a lower A_{UV} , and a lower M_* than the sample as a whole. These properties can be attributed to a population of highly star-forming, young galaxies that are still assembling the bulk of their stellar mass. These results suggest that galaxies exhibiting strong Mg II emission may be undergoing a transformation from bursty (i.e., high-sSFR), minimally-attenuated, low-mass objects to a more mature population in which attenuation by dust precludes observations of emission lines. Robust estimates of galaxy ages will be instrumental for testing the hypothesis that galaxies with strong Mg II emission lines represent a stage of galaxy evolution that perhaps a large fraction of the galaxy population evolves through. Probing the geometry and morphology of extended Mg II emission is additionally important for understanding the distribution of gas in and around galaxy halos.

While objects with strong Fe II* emission show some properties in common with Mg II emitters – i.e., larger $W_{[OII]}$ and lower A_{UV} – the dependencies of Fe II* and Mg II emission strengths on galaxy properties are not identical. In particular, Fe II* emission is not as closely linked with sSFR and M_* as Mg II emission is. Since sSFR and M_* trace star formation and the build-up of stellar mass, the tight relationship between these properties and Mg II strength would be expected if Mg II emission originated in star-forming regions (Erb et al. 2012). On the other hand, if Fe II* emission arises in galactic halos, as Giavalisco et al. (2011) suggest, then it would be surprising if Fe II* emission was strongly modulated by properties describing star-forming environments. Observations that Mg II emission is spatially extended (Martin et al. 2013; Erb et al. 2012) are not inconsistent with Mg II emission originating in star-forming clumps, as Mg II is a resonant line highly susceptible to scattering.

6.3. The Absence of Fe II* Emission in Local Samples

While Fe II* emission lines are prevalent in samples at $z \geq 0.5$, including star-forming and post-starburst galaxies, AGNs, and quasars (Wang et al. 2008; Coil et al. 2011; Giavalisco et al. 2011; Rubin et al. 2010a, 2011; Erb et al. 2012, this work), Fe II* emission is conspicuously absent in local starbursts. Figure 22 contrasts the composite spectrum of $z \sim 1$ star-forming galaxies from this work with a composite spectrum of $z \sim 0$ star-forming galaxies from Leitherer et al. (2011). One immediately notices the lack of Fe II* emission in the local sample⁹. Giavalisco et al. (2011) propose that spectra from nearby samples lack Fe II* emission due to slit losses. Given the small physical-to-angular conversion valid for the local universe – 170 pc/'' at the average redshift of the Leitherer et al. (2011) sample – spectroscopic

observations at $z \sim 0$ fail to encompass the halos of galaxies where Giavalisco et al. (2011) suggest Fe II* emission originates. Indeed, the Leitherer et al. (2011) observations target only small H II regions of size ~ 100 pc. Spectroscopic observations of distant galaxies, in comparison, are inclusive of extended emission given typical slit widths of $\sim 1''$ and physical-to-angular conversions of 8 kpc/'' at $z = 1$. The hypothesis that fine-structure emission originates in extended galaxy halos is supported by the results of Jones et al. (2012). These authors used a sample of 81 Lyman break galaxies at $z \sim 4$ to show that the equivalent width of a fine-structure Si II* emission line was significantly less than the equivalent width of its paired resonant Si II absorption line. One would expect that the equivalent widths of the fine-structure and resonant absorption lines to be equal if both features originated from similar spatial scales. The result that the emission has a smaller equivalent width is consistent with Si II* emission being more spatially extended than the resonant absorption and therefore falling beyond the spectroscopic slit. Other authors have also invoked slit losses to explain the absence of Si II* emission in local samples (e.g., Schwartz et al. 2006, but see France et al. 2010) while high-redshift ($z \sim 3$) observations show Si II* (e.g., Shapley et al. 2003). Since differences in A_{UV} are strongly linked to changes in Fe II* emission strength, as discussed above, it is important to note that there is redshift evolution in A_{UV} at a fixed SFR, such that objects at higher redshifts show less dust attenuation, on average (Adelberger & Steidel 2000). Therefore, the differences in Fe II* emission strength between local and $z \sim 1$ samples may be due both to slit losses and differences in dust attenuation.

If the frequency of detecting Fe II* emission depends on the spatial scale probed by spectroscopic observations, as Giavalisco et al. (2011) suggest, one would expect to see variation in the strength of Fe II* emission as a function of galaxy angular size. We used Petrosian radii – measured in the V band for objects at $z < 1.10$ and in the I band for objects at $z > 1.10$ – to divide the sample into two groups based on angular size. From composite spectra assembled from each group, we found that smaller objects ($\langle R_P \rangle = 0.''6$, where R_P is the Petrosian radius) showed $\sim 50\%$ stronger 2396 and 2626 Å Fe II* emission than larger ($\langle R_P \rangle = 1.''3$) objects, significant at the 1.8σ level (Figure 20). The average change in angular diameter distance between the two groups of objects is only 12%. While these results are consistent with Fe II* emission arising from spatially-extended winds, we caution that solely dividing galaxies on the basis of angular size is a blunt tool for analysis given the diversity of galaxies populating each angular size bin. Angular size is correlated with redshift at the 2.7σ level, and redshift is in turn correlated with SFR, A_{UV} , and $W_{[OII]}$ (Figure 10). In the absence of a larger sample, it is difficult to isolate objects that vary in angular size but do not vary significantly in other galaxy properties.

The lack of Fe II* emission in local samples has motivated the hypothesis that slit losses preclude observations of extended Fe II* emission in nearby galaxies. Prochaska et al. (2011) find that Fe II* emission is spatially extended with non-zero surface brightness at large galactocentric radii; a $1''$ slit covering a galaxy at $z >$

⁹ Mg II emission above the continuum is also absent in the Leitherer et al. (2011) composite spectrum, although obvious Mg II emission is likewise not present in the composite spectrum of our own data.

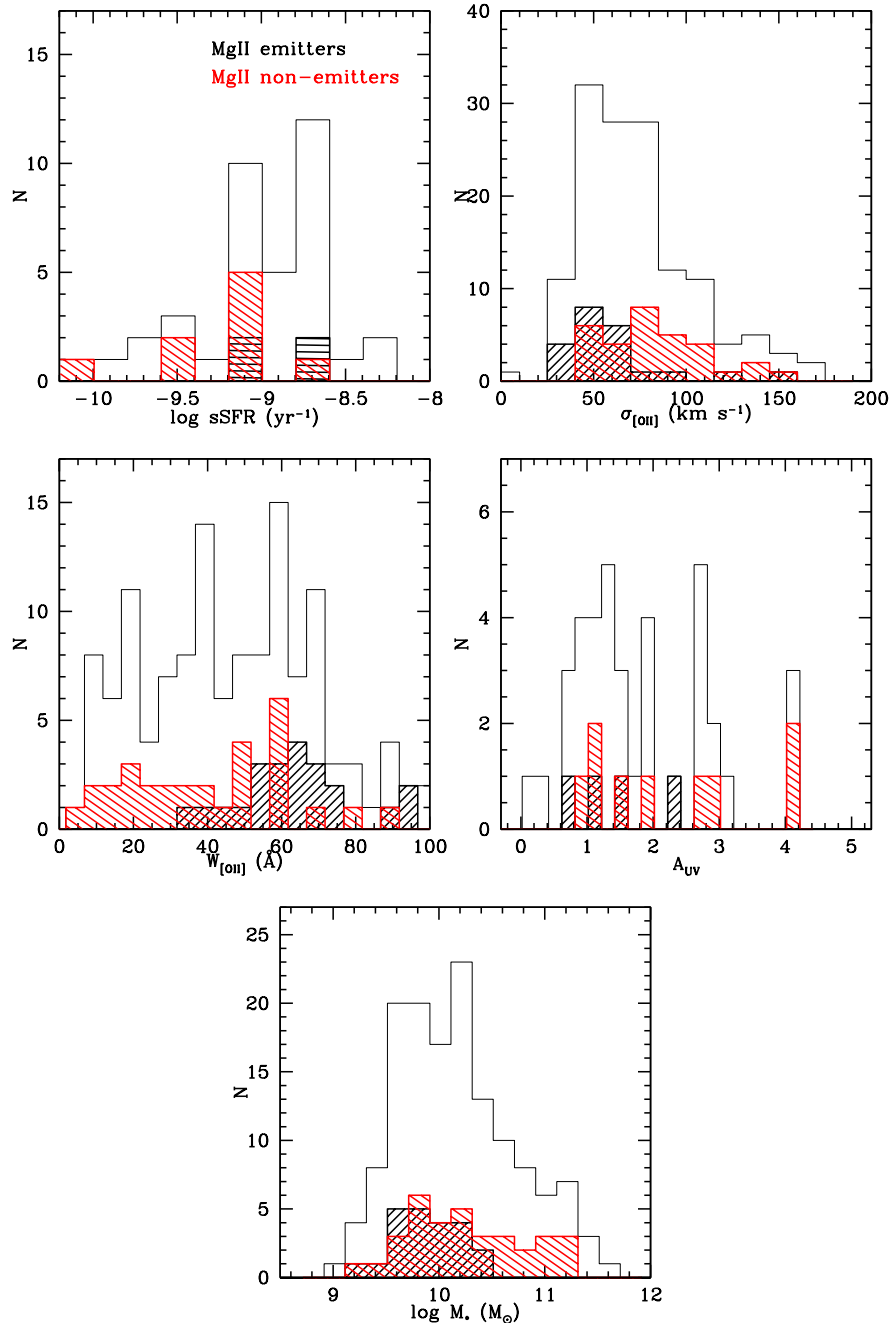


FIG. 18.— Histograms of five key parameters modulating Mg II emission strength: sSFR, $\sigma_{[\text{OII}]}$, $W_{[\text{OII}]}$, A_{UV} , and M_* . In each panel, the open histogram shows the parent sample of objects with $S/N > 4.66$. Mg II emitters are shown in the black shaded histogram and Mg II non-emitters are indicated with the red shaded histogram. Mg II emitters are characterized by higher sSFR, lower $\sigma_{[\text{OII}]}$, larger $W_{[\text{OII}]}$, lower A_{UV} , and lower M_* than Mg II non-emitters.

0.5 would include less than 50% of the Fe II* emission, assuming a spherically-symmetric wind. At lower redshifts, even less of the Fe II* emission would fall into the spectroscopic slit. While Prochaska et al. (2011) focus on Fe II* emission arising in the presence of gas flows, Fe II* lines are generated even in the absence of galactic winds. While not all objects in our sample show evidence for outflows, we used spatially-resolved imaging in Kornei et al. (2012) and outflow fraction calculations in Martin et al. (2012) to infer that the prevalence of out-

flows is likely modulated by galaxy inclination. All star-forming systems at $z \sim 1$ may in actuality drive outflows, but only a fraction of objects exhibit outflow signatures depending on the orientation of the outflowing wind with respect to the observer.

7. SUMMARY AND CONCLUSIONS

Fine-structure Fe II* and resonant Mg II emission lines, observable from the ground over a wide range of redshifts, are an important probe of gas flows. We have investigated the properties and prevalence of Fe II* and Mg II

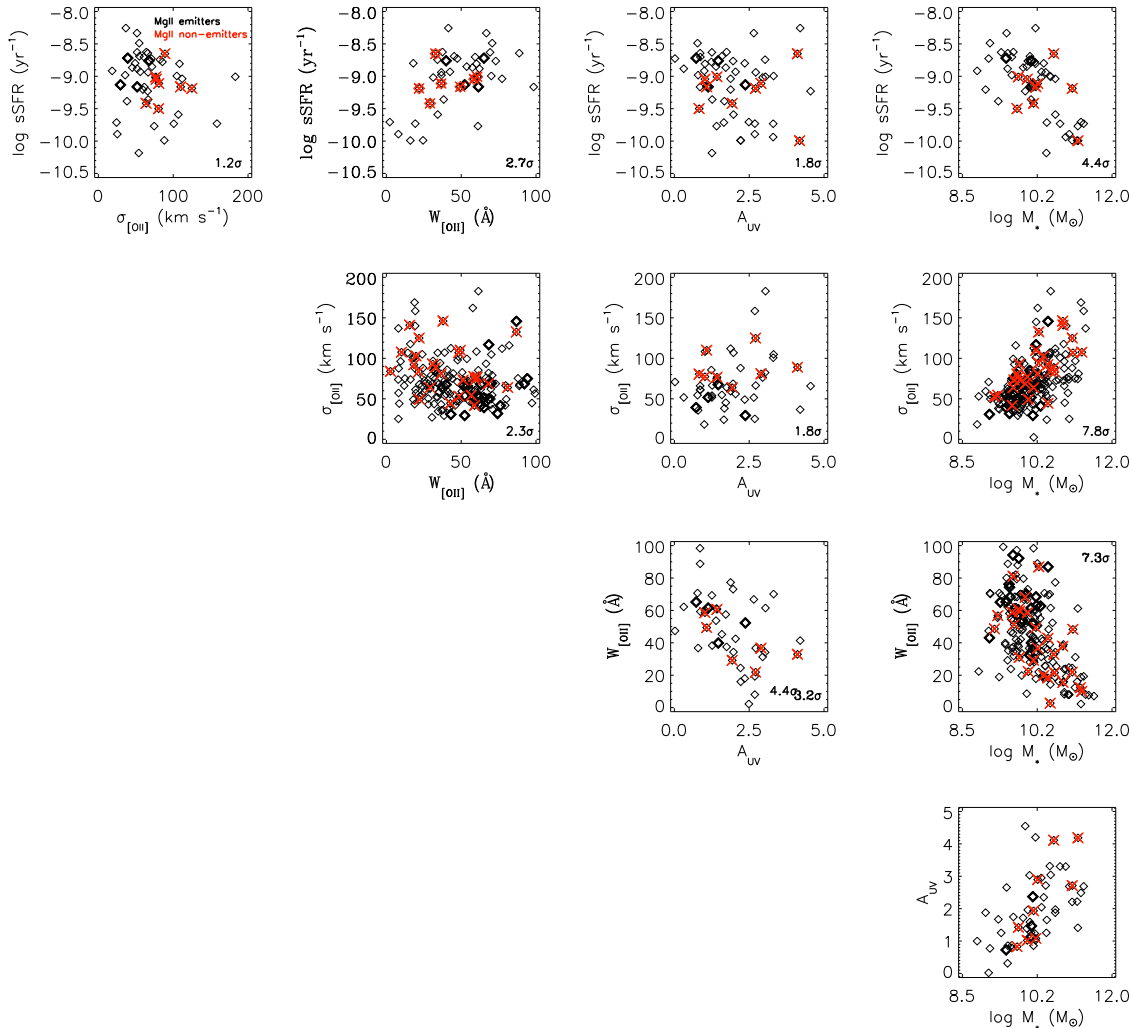


FIG. 19.— Intercorrelations of sSFR, $\sigma_{[\text{OII}]}$, $W_{[\text{OII}]}$, A_{UV} , and M_* . Mg II emitters are indicated with thick black diamonds and Mg II non-emitters are shown as red stars. We propose that both sSFR and A_{UV} strongly modulate Mg II emission, such that objects with stronger Mg II emission typically have lower sSFR and lower A_{UV} than objects with weak or absent Mg II emission.

emission in a sample of 212 star-forming galaxies at $z \sim 1$. We utilized LRIS rest-frame ultraviolet spectroscopy and a rich data set of *GALEX*, *HST*, and *Spitzer* imaging. Our study focused on the kinematics of Fe II* and Mg II emission and how the strength of these lines vary as a function of star-forming, gas flow, interstellar gas absorption, stellar population, size, morphological, and redshift properties. We provide below a numbered list of our main conclusions:

1. Fe II* emission is prevalent at $z \sim 1$ in composite spectra assembled from a range of galaxy properties, although Fe II* emission is not observed in local studies probing star-forming regions. This absence of Fe II* emission in nearby samples may be due to slit losses.

2. The centroids of the strongest Fe II* emission lines are consistent with the systemic velocity of the galaxy and Fe II* emission may consequently originate either in the disk of the galaxy or in a spatially-extended outflowing wind.

3. Fe II* emission is primarily modulated by A_{UV} , where less dusty systems show stronger Fe II* emission.

Objects selected on the basis of strong Fe II* emission also tend to show stronger Fe II resonant absorption, although we caution that this effect may be primarily driven by redshift evolution as Fe II* emitters are preferentially at higher redshifts than Fe II* non-emitters in our sample.

4. Mg II emission is most pronounced in systems with higher sSFR, lower A_{UV} , and lower M_* . We find the strongest correlation between Mg II emission strength and sSFR.

We have demonstrated that galaxies with strong Fe II* or Mg II emission have typically higher sSFR, lower A_{UV} , and lower M_* than the sample as a whole. These objects may accordingly represent a bursty (i.e., high-sSFR), minimally-attenuated, low-mass stage of galaxy evolution. Future studies of emission in star-forming galaxies will benefit from targeted searches of galaxies with higher sSFR, lower A_{UV} , and lower M_* properties. As Fe II* is thought to originate in extended galaxy halos and the A_{UV} values measured in this study reflect the attenuation toward H II regions, upcoming work will be nec-

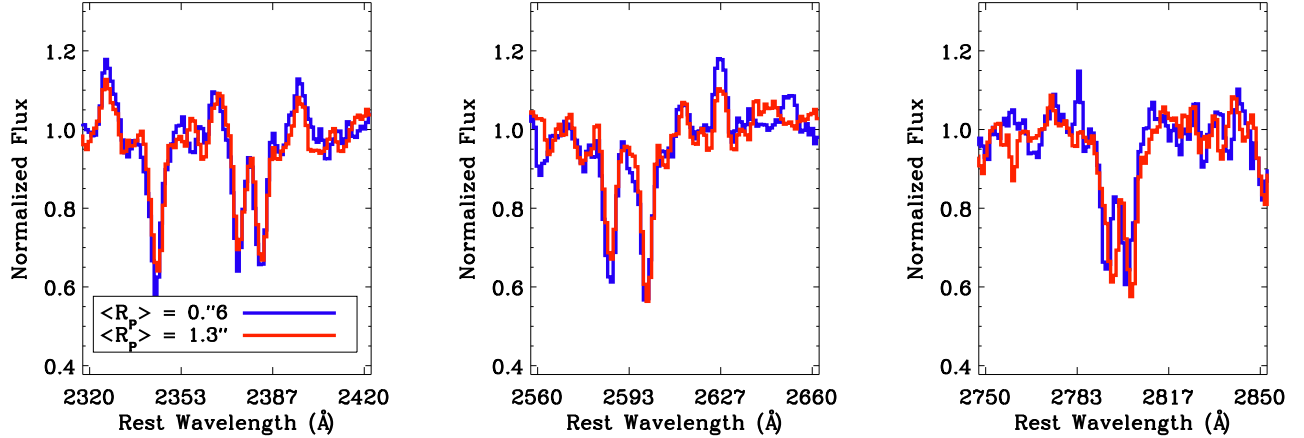


FIG. 20.— Composite spectra assembled on the basis of angular Petrosian radius. The stack of smaller objects ($\langle R_P \rangle = 0.''6$) is shown in blue while the composite spectrum comprised of larger objects ($\langle R_P \rangle = 1.3''$) is shown in red. Typical errors on both composite spectra are ~ 0.04 , in normalized flux units. Smaller objects show stronger 2396 and 2626 Å Fe II* emission than larger objects at the 1.8σ level, an indication that our data are consistent with the theory of Fe II* emission slit losses presented by Giallisco et al. (2011) and Erb et al. (2012). Smaller objects also exhibit more blueshifted Mg II centroids, analogous to the results of Law et al. (2012) for a sample of star-forming galaxies at $z = 1.5$ – 3.6 .

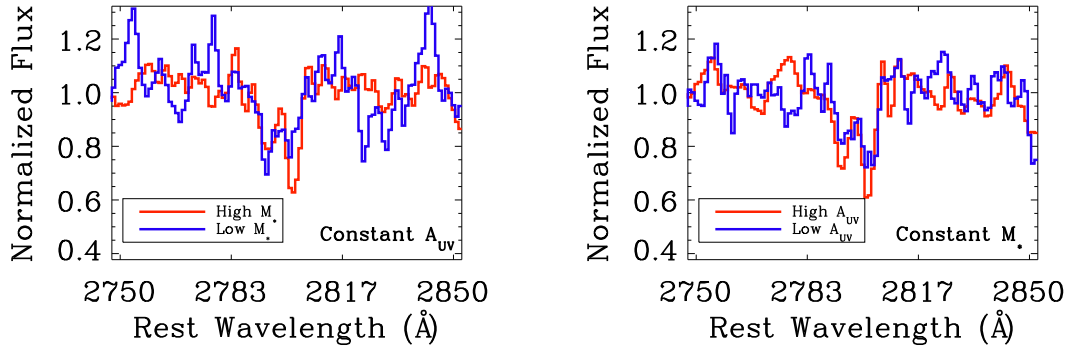


FIG. 21.— Mg II profiles of composite spectra assembled holding M_* (A_{UV}) constant and varying A_{UV} (M_*). Mg II variation is seen in both pairs of composite spectra, indicating that both M_* and A_{UV} modulate Mg II. However, the composite spectra divided by A_{UV} show stronger and more consistent variation in their Mg II profiles ($D_{MgII} = 0.71$ Å) than the composite spectra divided by M_* ($D_{MgII} = 0.00$ Å), suggestive that A_{UV} modulates Mg II more strongly than M_* . It is important to acknowledge that these composite spectra were each assembled from fewer than 10 individual spectra and are accordingly of lower S/N than the majority of the composite spectra in this paper.

essary for understanding the relationship between dust in star-forming regions and dust at larger galactocentric distances.

Investigations of the spatial and morphological properties of galactic winds in emission – information that is lacking from most current long-slit spectroscopic observations – are critical for detailed modeling of outflows and testing of non-spherically symmetric models of galactic winds. Several studies thus far have offered tantalizing evidence that resonant and fine-structure emission may be spatially extended beyond the stellar continuum, although larger sample sizes are needed. New instrumentation such as KCWI and MUSE will yield data on the three dimensional structure of gas flows. Upcoming observations with these instruments will be important for understanding the enrichment of the circumgalactic medium and the connections between galaxies and their environments.

We thank Kevin Hainline for providing code used in our Monte Carlo simulations. K.A.K. is grateful for support from a UCLA Dissertation Year Fellowship. A.E.S. acknowledges support from the David and Lucile Packard Foundation. This study was supported in part by the NSF under contract AST-0909182 (C.L.M.). A portion of this work was completed at the Aspen Center for Physics (C.L.M.). The Alfred P. Sloan Foundation and an NSF CAREER award (AST-1055081) supported A.L.C. This study makes use of data from AEGIS, a multiwavelength sky survey conducted with the *Chandra*, *GALEX*, *Hubble*, Keck, CFHT, MMT, Subaru, Palomar, *Spitzer*, VLA, and other telescopes and supported in part by the NSF, NASA, and the STFC. We also recognize and acknowledge the very significant cultural role and reverence that the summit of Mauna Kea has always had within the indigenous Hawaiian community. We are most fortunate to have the opportunity to conduct observations from this mountain.

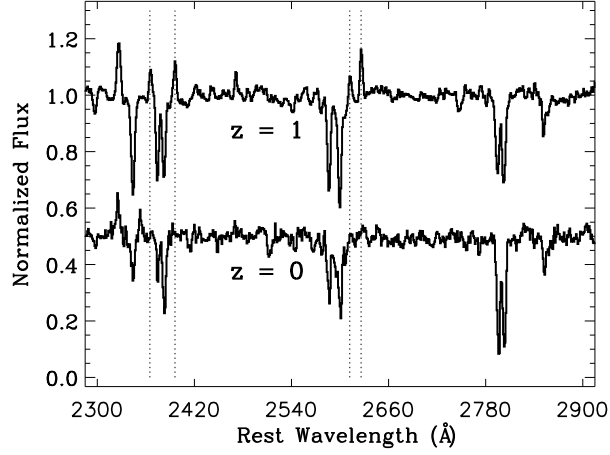


FIG. 22.— Comparison of composite spectra of star-forming galaxies at $z \sim 1$ (this work) and $z \sim 0$ (Leitherer et al. 2011). Fe II* emission (vertical dotted lines) is conspicuous in the $z \sim 1$ sample while the $z \sim 0$ sample (28 local star-forming galaxies observed in 46 unique pointings) does not show Fe II* emission. Giavalisco et al. (2011) and Erb et al. (2012) hypothesize that slit losses may be responsible for the lack of Fe II* emission in nearby samples. As the Leitherer et al. (2011) pointings target very small spatial scales (starburst regions of size ~ 100 pc), spatially-extended Fe II* emission would be missed by these observations. Spectroscopic observations of galaxies at $z \sim 1$, on the other hand, typically encompass the entire galaxy given the physical-to-angular conversion of ~ 8 kpc $''$.

REFERENCES

- Adelberger, K. L., & Steidel, C. C. 2000, *ApJ*, 544, 218
- Bacon, R., Accardo, M., Adjali, L., Anwand, H., Bauer, S., Biswas, I., Blaizot, J., Boudon, D., Brau-Nogue, S., Brinchmann, J., Caillier, P., Capoani, L., Carollo, C. M., Contini, T., Couderc, P., Daguisé, E., Deiries, S., Delabre, B., Dreizler, S., Dubois, J., Dupieux, M., Dupuy, C., Emsellem, E., Fechner, T., Fleischmann, A., François, M., Gallou, G., Gharsa, T., Glindemann, A., Gojak, D., Guiderdoni, B., Hansali, G., Hahn, T., Jarno, A., Kelz, A., Koehler, C., Kosmalski, J., Laurent, F., Le Floch, M., Lilly, S. J., Lizon, J.-L., Loupiau, M., Manescau, A., Monstein, C., Nicklas, H., Olaya, J.-C., Pares, L., Pasquini, L., Pécontal-Rousset, A., Pelló, R., Petit, C., Popow, E., Reiss, R., Remillieux, A., Renault, E., Roth, M., Rupprecht, G., Serre, D., Schaye, J., Soucail, G., Steinmetz, M., Streicher, O., Stuijk, R., Valentin, H., Vernet, J., Weilbacher, P., Wisotzki, L., & Yerle, N. 2010, in *Society of Photo-Optical Instrumentation Engineers (SPIE) Conference Series*, Vol. 7735, *Society of Photo-Optical Instrumentation Engineers (SPIE) Conference Series*
- Bordoloi, R., Lilly, S. J., Knobel, C., Bolzonella, M., Kampeczyk, P., Carollo, C. M., Iovino, A., Zucca, E., Contini, T., Kneib, J.-P., Le Fevre, O., Mainieri, V., Renzini, A., Scoddeggio, M., Zamorani, G., Balestra, I., Bardelli, S., Bongiorno, A., Caputi, K., Cucciati, O., de la Torre, S., de Ravel, L., Garilli, B., Kovač, K., Lamareille, F., Le Borgne, J.-F., Le Brun, V., Maier, C., Mignoli, M., Pello, R., Peng, Y., Perez Montero, E., Pratto, V., Scarlata, C., Silverman, J., Tanaka, M., Tasca, L., Tresse, L., Vergani, D., Barnes, L., Cappi, A., Cimatti, A., Coppa, G., Diener, C., Franzetti, P., Koekemoer, A., López-Sanjuan, C., McCracken, H. J., Moresco, M., Nair, P., Oesch, P., Pozzetti, L., & Welikala, N. 2011, *ApJ*, 743, 10
- Brinchmann, J., Charlot, S., White, S. D. M., Tremonti, C., Kauffmann, G., Heckman, T., & Brinkmann, J. 2004, *MNRAS*, 351, 1151
- Bruzual, G., & Charlot, S. 2003, *MNRAS*, 344, 1000
- Calzetti, D., Armus, L., Bohlin, R. C., Kinney, A. L., Koornneef, J., & Storchi-Bergmann, T. 2000, *ApJ*, 533, 682
- Chabrier, G. 2003, *PASP*, 115, 763
- Coil, A. L., Weiner, B. J., Holz, D. E., Cooper, M. C., Yan, R., & Aird, J. 2011, *ApJ*, 743, 46
- Davis, M., Guhathakurta, P., Konidaris, N. P., Newman, J. A., Ashby, M. L. N., Biggs, A. D., Barmby, P., Bundy, K., Chapman, S. C., Coil, A. L., Conselice, C. J., Cooper, M. C., Croton, D. J., Eisenhardt, P. R. M., Ellis, R. S., Faber, S. M., Fang, T., Fazio, G. G., Georgakakis, A., Gerke, B. F., Goss, W. M., Gwyn, S., Harker, J., Hopkins, A. M., Huang, J., Ivison, R. J., Kassin, S. A., Kirby, E. N., Koekemoer, A. M., Koo, D. C., Laird, E. S., Le Floch, E., Lin, L., Lotz, J. M., Marshall, P. J., Martin, D. C., Metevier, A. J., Moustakas, L. A., Nandra, K., Noeske, K. G., Papovich, C., Phillips, A. C., Rich, R. M., Rieke, G. H., Rigopoulou, D., Salim, S., Schiminovich, D., Simard, L., Smail, I., Small, T. A., Weiner, B. J., Willmer, C. N. A., Willner, S. P., Wilson, G., Wright, E. L., & Yan, R. 2007, *ApJ*, 660, L1
- Erb, D. K., Quider, A. M., Henry, A. L., & Martin, C. L. 2012, *ApJ*, 759, 26
- Erb, D. K., Shapley, A. E., Pettini, M., Steidel, C. C., Reddy, N. A., & Adelberger, K. L. 2006, *ApJ*, 644, 813
- France, K., Nell, N., Green, J. C., & Leitherer, C. 2010, *ApJ*, 722, L80
- Franx, M., Illingworth, G. D., Kelson, D. D., van Dokkum, P. G., & Tran, K. 1997, *ApJ*, 486, L75
- Gabor, J. M., Davé, R., Oppenheimer, B. D., & Finlator, K. 2011, *MNRAS*, 417, 2676
- Genzel, R., Newman, S., Jones, T., Förster Schreiber, N. M., Shapiro, K., Genel, S., Lilly, S. J., Renzini, A., Tacconi, L. J., Bouché, N., Burkert, A., Cresci, G., Buschkamp, P., Carollo, C. M., Ceverino, D., Davies, R., Dekel, A., Eisenhauer, F., Hicks, E., Kurk, J., Lutz, D., Mancini, C., Naab, T., Peng, Y., Sternberg, A., Vergani, D., & Zamorani, G. 2011, *ApJ*, 733, 101
- Giavalisco, M., Vanzella, E., Salimbeni, S., Tripp, T. M., Dickinson, M., Cassata, P., Renzini, A., Guo, Y., Ferguson, H. C., Nonino, M., Cimatti, A., Kurk, J., Mignoli, M., Tang, Y., & . 2011, *ApJ*, 743, 95
- Heckman, T. M., Armus, L., & Miley, G. K. 1990, *ApJS*, 74, 833
- Heckman, T. M., Lehnert, M. D., Strickland, D. K., & Armus, L. 2000, *ApJS*, 129, 493
- Holwerda, B. W., Keel, W. C., Williams, B., Dalcanton, J. J., & de Jong, R. S. 2009, *AJ*, 137, 3000
- Jones, T., Stark, D. P., & Ellis, R. S. 2012, *ApJ*, 751, 51
- Kinney, A. L., Bohlin, R. C., Calzetti, D., Panagia, N., & Wyse, R. F. G. 1993, *ApJS*, 86, 5
- Kornei, K. A., Shapley, A. E., Erb, D. K., Steidel, C. C., Reddy, N. A., Pettini, M., & Bogosavljević, M. 2010, *ApJ*, 711, 693
- Kornei, K. A., Shapley, A. E., Martin, C. L., Coil, A. L., Lotz, J. M., Schiminovich, D., Bundy, K., & Noeske, K. G. 2012, *ApJ*, 758, 135
- Kurk, J., Cimatti, A., Daddi, E., Mignoli, M., Pozzetti, L., Dickinson, M., Bolzonella, M., Zamorani, G., Cassata, P., Rodighiero, G., Franceschini, A., Renzini, A., Rosati, P., Halliday, C., & Berta, S. 2013, *A&A*, 549, A63
- Law, D. R., Steidel, C. C., Erb, D. K., Pettini, M., Reddy, N. A., Shapley, A. E., Adelberger, K. L., & Simenc, D. J. 2007, *ApJ*, 656, 1
- Law, D. R., Steidel, C. C., Shapley, A. E., Nagy, S. R., Reddy, N. A., & Erb, D. K. 2012, *ApJ*, 759, 29
- Lehnert, M. D., & Heckman, T. M. 1996, *ApJ*, 462, 651
- Leitherer, C., Tremonti, C. A., Heckman, T. M., & Calzetti, D. 2011, *AJ*, 141, 37
- Lotz, J. M., Primack, J., & Madau, P. 2004, *AJ*, 128, 163
- Martin, C., Moore, A., Morrissey, P., Matuszewski, M., Rahman, S., Adkins, S., & Epps, H. 2010, in *Society of Photo-Optical Instrumentation Engineers (SPIE) Conference Series*, Vol. 7735, *Society of Photo-Optical Instrumentation Engineers (SPIE) Conference Series*
- Martin, C. L. 1998, *ApJ*, 506, 222
- . 1999, *ApJ*, 513, 156
- . 2005, *ApJ*, 621, 227
- Martin, C. L., & Bouché, N. 2009, *ApJ*, 703, 1394
- Martin, C. L., Shapley, A. E., Coil, A. L., Kornei, K. A., Bundy, K., Weiner, B. J., Noeske, K. G., & Schiminovich, D. 2012, *ApJ*, 760, 127
- Martin, C. L., Shapley, A. E., Coil, A. L., Kornei, K. A., Murray, N., & Pancoast, A. 2013, *ApJ*, accepted (astro-ph/1304.6405)
- Martin, D. C., Wyder, T. K., Schiminovich, D., Barlow, T. A., Forster, K., Friedman, P. G., Morrissey, P., Neff, S. G., Seibert, M., Small, T., Welsh, B. Y., Bianchi, L., Donas, J., Heckman, T. M., Lee, Y.-W., Madore, B. F., Milliard, B., Rich, R. M., Szalay, A. S., & Yi, S. K. 2007, *ApJS*, 173, 342
- Ménard, B., Scranton, R., Fukugita, M., & Richards, G. 2010, *MNRAS*, 405, 1025
- Ménard, B., Wild, V., Nestor, D., Quider, A., Zibetti, S., Rao, S., & Turnshek, D. 2011, *MNRAS*, 417, 801
- Nelson, A. E., Zaritsky, D., & Cutri, R. M. 1998, *AJ*, 115, 2273
- Newman, J. A., Cooper, M. C., Davis, M., Faber, S. M., Coil, A. L., Guhathakurta, P., Koo, D. C., Phillips, A. C., Conroy, C., Dutton, A. A., Finkbeiner, D. P., Gerke, B. F., Rosario, D. J., Weiner, B. J., Willmer, C. N. A., Yan, R., Harker, J. J., Kassin, S. A., Konidaris, N. P., Lai, K., Madgwick, D. S., Noeske, K. G., Wirth, G. D., Connolly, A. J., Kaiser, N., Kirby, E. N., Lemaux, B. C., Lin, L., Lotz, J. M., Luppino, G. A., Marinoni, C., Matthews, D. J., Metevier, A., & Schiavon, R. P. 2012, *ApJ*, submitted (astro-ph/1203.3192)
- Pettini, M., Shapley, A. E., Steidel, C. C., Cuby, J., Dickinson, M., Moorwood, A. F. M., Adelberger, K. L., & Giavalisco, M. 2001, *ApJ*, 554, 981
- Pettini, M., Steidel, C. C., Adelberger, K. L., Dickinson, M., & Giavalisco, M. 2000, *ApJ*, 528, 96
- Phillips, A. C. 1993, *AJ*, 105, 486
- Prochaska, J. X., Kasen, D., & Rubin, K. 2011, *ApJ*, 734, 24
- Ralchenko, Y., Fuhr, J. R., Jou, F.-C., Kramida, A. E., Martin, W. C., Podobedova, L. I., Reader, J., Saloman, E. B., Sansonetti, J. E., & Wiese, W. L. 2005, in *American Institute of Physics Conference Series*, Vol. 771, *Atomic and Molecular Data and their Applications*, ed. T. Kato, D. Kato, & H. Funaba, 276–285
- Rubin, K. H. R., Prochaska, J. X., Koo, D. C., Phillips, A. C., & Weiner, B. J. 2010a, *ApJ*, 712, 574
- Rubin, K. H. R., Prochaska, J. X., Ménard, B., Murray, N., Kasen, D., Koo, D. C., & Phillips, A. C. 2011, *ApJ*, 728, 55

- Rubin, K. H. R., Weiner, B. J., Koo, D. C., Martin, C. L., Prochaska, J. X., Coil, A. L., & Newman, J. A. 2010b, *ApJ*, 719, 1503
- Rupke, D. S., Veilleux, S., & Sanders, D. B. 2005, *ApJS*, 160, 115
- Sato, T., Martin, C. L., Noeske, K. G., Koo, D. C., & Lotz, J. M. 2009, *ApJ*, 696, 214
- Savage, B. D., & Sembach, K. R. 1996, *ARA&A*, 34, 279
- Schwartz, C. M., Martin, C. L., Chandar, R., Leitherer, C., Heckman, T. M., & Oey, M. S. 2006, *ApJ*, 646, 858
- Seibert, M., Martin, D. C., Heckman, T. M., Buat, V., Hoopes, C., Barlow, T., Bianchi, L., Byun, Y., Donas, J., Forster, K., Friedman, P. G., Jelinsky, P., Lee, Y., Madore, B. F., Malina, R., Milliard, B., Morrissey, P., Neff, S., Rich, R. M., Schiminovich, D., Morrissey, P., Neff, S., Rich, R. M., Schiminovich, D., & Wyder, T. K. 2005, *ApJ*, 619, L55
- Shapley, A. E., Steidel, C. C., Pettini, M., & Adelberger, K. L. 2003, *ApJ*, 588, 65
- Steidel, C. C., Erb, D. K., Shapley, A. E., Pettini, M., Reddy, N., Bogosavljević, M., Rudie, G. C., & Rakic, O. 2010, *ApJ*, 717, 289
- Steidel, C. C., Giavalisco, M., Pettini, M., Dickinson, M., & Adelberger, K. L. 1996, *ApJ*, 462, L17
- Talia, M., Mignoli, M., Cimatti, A., Kurk, J., Berta, S., Bolzonella, M., Cassata, P., Daddi, E., Dickinson, M., Franceschini, A., Halliday, C., Pozzetti, L., Renzini, A., Rodighiero, G., Rosati, P., & Zamorani, G. 2012, *A&A*, 539, A61
- Tremonti, C. A., Heckman, T. M., Kauffmann, G., Brinchmann, J., Charlot, S., White, S. D. M., Seibert, M., Peng, E. W., Schlegel, D. J., Uomoto, A., Fukugita, M., & Brinkmann, J. 2004, *ApJ*, 613, 898
- Tremonti, C. A., Moustakas, J., & Diamond-Stanic, A. M. 2007, *ApJ*, 663, L77
- Veilleux, S., Cecil, G., & Bland-Hawthorn, J. 2005, *ARA&A*, 43, 769
- Verhamme, A., Schaerer, D., & Maselli, A. 2006, *A&A*, 460, 397
- Wang, T., Dai, H., & Zhou, H. 2008, *ApJ*, 674, 668
- Weiner, B. J., Coil, A. L., Prochaska, J. X., Newman, J. A., Cooper, M. C., Bundy, K., Conselice, C. J., Dutton, A. A., Faber, S. M., Koo, D. C., Lotz, J. M., Rieke, G. H., & Rubin, K. H. R. 2009, *ApJ*, 692, 187
- Willmer, C. N. A., Faber, S. M., Koo, D. C., Weiner, B. J., Newman, J. A., Coil, A. L., Connolly, A. J., Conroy, C., Cooper, M. C., Davis, M., Finkbeiner, D. P., Gerke, B. F., Guhathakurta, P., Harker, J., Kaiser, N., Kassin, S., Konidaris, N. P., Lin, L., Luppino, G., Madgwick, D. S., Noeske, K. G., Phillips, A. C., & Yan, R. 2006, *ApJ*, 647, 853
- Wright, E. L. 2006, *PASP*, 118, 1711
- Wu, C., Boggess, A., & Gull, T. R. 1983, *ApJ*, 266, 28